Evaluation of Simulated Marine Aerosol Production Using the WaveWatchIII Prognostic Wave Model Coupled to the Community Atmosphere Model within the Community Earth System Model

M.S. Long – Harvard John A. Paulson School of Engineering and Applied Sciences, Cambridge, MA USA (corresponding author: mlong@seas.harvard.edu)
W.C. Keene – University of Virginia Department of Environmental Sciences, Charlottesville, VA USA
J. Zhang – University of North Dakota Department of Atmospheric Sciences, Grand Forks, ND USA
B. Reichl – University of Rhode Island Graduate School of Oceanography, Narragansett, RI USA
Y. Shi – University of North Dakota Department of Atmospheric Sciences, Grand Forks, ND USA
T. Hara – University of Rhode Island Graduate School of Oceanography, Narragansett, RI USA
J. S. Reid – Naval Research Laboratory, Monterey, CA USA, 93907
B. Fox-Kemper – Brown University Earth, Environmental and Planetary Sciences, Providence, RI USA
A. P. Craig – National Center for Atmospheric Research, Boulder, CO USA
D.J. Erickson - Computer Science and Mathematics Division, Oak Ridge National Laboratory, Oak Ridge, TN, USA
I. Ginis – University of Rhode Island Graduate School of Oceanography, Narragansett, RI USA
A. Webb - University of Tokyo Department of Ocean Technology, Policy, and Environment, Tokyo, Japan

Submitted to the *Journal of Geophysical Research*

Key Points: (1) Marine aerosol emission scales with prognostic wind-wave model. (2) 10-meter wind speed unable to capture basin-scale wind-wave properties. (3) Wave-based aerosol emission did not improve comparison to observed particulate Na^+.

Abstract

Primary marine aerosol (PMA) is emitted into the atmosphere via breaking wind waves on the ocean surface. Most parameterizations of PMA emissions use 10-meter wind speed as a proxy for wave action. This investigation coupled the 3rd generation prognostic WAVEWATCH-III wind-wave model within a coupled Earth system model (ESM) to drive PMA production using wave energy dissipation rate – analogous to whitecapping – in place of 10-meter wind speed. The wind speed parameterization did not capture basin-scale variability in relations between wind and wave fields. Overall, the wave parameterization did not improve comparison between simulated versus measured AOD or Na^+, thus highlighting large remaining uncertainties in model physics. Results confirm the efficacy of prognostic wind-wave models for air-sea exchange studies coupled with laboratory- and field-based characterizations of the primary physical drivers of PMA production. No discernible correlations were evident between simulated PMA fields and observed chlorophyll or sea surface temperature.

1. Introduction

Particle production by bursting bubbles at the air-sea interface is the dominant global source of aerosol mass and a major global source of aerosol number (Andreae and Rosenfeld, 2008). Primary marine aerosol (PMA) is an important composition-dependent reaction medium that influences the multiphase physicochemical evolution of the marine troposphere [*von Glasow and Crutzen*, 2004; *Long et al.*, 2014a]. These particles are highly enriched (typically by 2 to 3 orders of magnitude based on bulk composition) in marine-derived organic matter (OM) [*Hoffman and Duce*, 1976; *Keene et al.*, 2007; *Facchini et al.*, 2008] the chemical processing of which is a significant source of the OH radical, hydroperoxides, and probably other low molecular weight reaction products including carboxylic acids, ketones, and alcohols [*Zhou et al.*, 2008]. PMA also scatters incident solar radiation and accounts for significant fractions of cloud condensation nuclei (CCN) over the world's oceans thereby influencing Earth's radiative balance and climate [*Clarke et al.*, 2006; *Pierce and Adams,* 2006; *Quinn and Bates*, 2011].

Despite their global significance, the size-resolved physical (mass and number) and chemical (organic and inorganic) properties and production fluxes of PMA are not adequately parameterized in comprehensive Earth system models as functions of major drivers (wind and wave fields and the chemical and physical characteristics of surface seawater). Some parameterizations are based on *in situ* measurements which are advantageous in that they directly relate variability in PMA production rates as inferred from ambient aerosol concentrations to the corresponding environmental drivers (e.g. wind speed). These include parameterizations based on measured number size distributions in near-surface marine air [*Gong*, 2003], vertical gradients in number size distributions measured immediately downwind of coastal surf [*Clarke et al.*, 2006], gradients in offshore flow regimes [*Reid et al.*, 2001], and eddy covariance measurements of sub-μm number concentrations during onshore flow [*Geever et al.*, 2005] and associated measurements of ambient aerosol composition [*Rinaldi et al.*, 2013]. However, these and other measurement techniques for ambient marine aerosol cannot reliably characterize size-resolved properties over the full relevant size range at high temporal resolution [*Reid et al.*, 2006]. In addition, size distributions of freshly produced PMA change rapidly (minutes to hours) in response to variable size-dependent dry-deposition

rates and meteorological conditions [*Keene et al.*, 2009]; and the corresponding chemical compositions change rapidly (seconds to minutes) via exposure to light and reactive trace gases [*Chameides and Stelson*, 1992; *Erickson et al.*, 1999; *Zhou et al.*, 2008]. PMA are also injected onto air already populated with aged particles that exhibit variable degrees of physicochemical modification, and (in many regions) contain components from non-marine sources (e.g. *Clarke et al.*, [2013]) . Consequently, it is extremely difficult to reliably deconvolve the characteristics of freshly produced versus aged aerosols based on measurements in ambient marine air.

Other recently published parameterizations have been developed based on aerosols generated artificially by bubbling air through or impinging water jets onto surfaces of natural or synthetic seawater. However, some of these studies consider only the sub-µm-diameter size fractions [*Sellegri et al.*, 2006; *Tyree et al.*, 2007; *Hultin et al.*, 2010] thereby ignoring the larger aerosols that dominate the mass and volume flux. In addition, aerosol produced from commercial synthetic seawater [e.g. *Mårtensson et al.*, 2003] or synthetic or natural seawater amended with addition of organic surfactant concentrations and compositions that are not representative of ambient seawater [e.g., *Modini et al.*, 2013] may not be representative of PMA produced from ambient seawater. The reader is referred to [*Hultin et al.*, 2010] for an intercomparison of normalized number size distributions reported by the above investigators. Spatial and temporal variability in cycling and impacts of size-resolved marine aerosols have also been simulated globally using models incorporating PMA production parameterizations based on results of some of the above studies (e.g., [*Pierce and Adams*, 2006; *Langmann et al.*, 2008; *Roelofs*, 2008; *Spracklen et al.*, 2008; *Gantt et al.*, 2009; *Long et al.*, 2014b]).

Most parameterizations of PMA production rely upon 10-m wind speed as a proxy for wave action. However, this approach cannot account for important non-linear processes involving wind waves that are not in equilibrium with local conditions, as is more commonly the case [*Hanley et al.*, 2010; *Webb and Fox-Kemper*, 2011; *Edson et al.*, 2013]. Several previous investigations of links between PMA emissions and wind-wave characteristics have focused on the wave-roughness Reynolds number [*Norris et al.*, 2013; *Partanen et al.*, 2014], which demonstrated better skill than wind speed alone in reproducing observations. We report herein a new approach using a prognostic wind-

wave model to simulate air entrainment into the surface ocean by breaking wind waves coupled with measured characteristics of size-resolved aerosols over full size distributions that were produced via the detrainment of artificially generated bubbles from fresh and artificial seawater under controlled conditions [*Mårtensson et al.*, 2003; *Keene et al.*, 2007; *Facchini et al.*, 2008; *Long et al.*, 2014]. This effort builds on prior work that parameterized PMA production based on the energetics of wind-wave breaking [*Long et al.*, 2011]. We examine the sensitivity of simulated PMA production, PMA burden, and associated first-order radiative impacts to the nature of the source function based on results from production parameterizations driven by wind speed versus those driven by the wind wave model. Simulated results are compared to measurements of ambient marine aerosol mass and optical depth. This work is part of a larger effort to develop, within the NCAR Community Atmosphere Model (CAM) component of the Community Earth System Model (CESM), a more explicit description of the sources, multiphase processing, and climatic interactions of naturally produced aerosols.

2. Methods

2.1 Models

Atmospheric processes were simulated in three dimensions (3-D) using the Community Atmosphere Model (CAM, version 5.3.16 [*Gent et al.*, 2009]) as part of Community Earth System Model (CESM, version 1.3; [*Hurrell et al.*, 2013]). Version 3.14 of the NOAA WAVEWATCH-III (WWIII) third-generation ocean wind-wave model [*Tolman*, 2009] was included as a separate component within the standard CESM to simulate wave fields for PMA emissions. WWIII solves the wave-number and direction resolved wind-wave energy spectrum on an Eulerian grid. The energy source term includes inputs from wind action on the ocean surface, dissipation from wave breaking, non-linear wave-wave interactions, interactions with the ocean bottom, depth-induced breaking, and terrain-based wave scattering. Zonal and meridional wind and ocean current velocities, sea-surface temperature (SST), and air temperature at 2 m were passed from CESM to the WWIII component. CESM's default ocean surface roughness parameters were used for momentum flux and atmospheric boundary layer calculations.

WWIII operates in the CESM similarly to the atmosphere, ocean, sea ice, land, land-ice,

and runoff components via communication within the hub-and-spoke coupled system. A top-level driver sequences all components (including WWIII) by calling component-specific initialization, run, and final interfaces. Fields are passed into and out of components via these interfaces, and all coupling fields are passed between models via the central "hub" coupler component. Synchronous restarts (from initial conditions saved from previous model executions) and time coordination in components are handled through the interface to the driver. The CESM was configured with online atmosphere and land model components, and was initialized at 1 January 2000. All other components were run in offline ('data') mode. To reduce model spin-up time, the sea-surface temperature was based on offline data for the 2000 calendar year and was cycled annually based on the NOAA Reynolds' SST climatology [*Reynolds et al.*, 2002, 2007]. Enhanced ocean mixing from prognostic waves (Q. Li, A. Webb, B. Fox-Kemper, A. Craig, G. Danabasoglu, W. G. Large, and M. Vertenstein, Langmuir mixing effects on global climate: WAVEWATCH III in CESM. Submitted to Ocean Modelling, 2015) was not active in this version of the model.

2.2 Marine Aerosol Source

Observations indicate that the total number production flux of PMA (F_T; $m^{-2}\ s^{-1}$) via bursting bubbles at the seawater surface is linearly proportional to the flux of air detrained from the water column [*Keene et al.*, 2007]. Measurements demonstrate that the total volume of air entrained within the water column by breaking waves (V_0 in m^3) is proportional to the energy dissipated by the wind-wave field through wave breaking (E_D in J; [*Lamarre and Melville*, 1991; *Loewen and Melville*, 1994; *Hoque*, 2002; *Blenkinsopp and Chaplin*, 2007]). Therefore, assuming that all air entrained into the water column detrains as bubbles that produce particles and neglecting impacts of surface-active material in seawater on bubble plume dynamics, the number production flux of marine aerosol can be estimated from the corresponding energy dissipated by wave breaking. The dissipation of wave energy by wave breaking involves work against the buoyant force of air entrained into the water column. Although the physical characteristics of plunging versus spilling breakers differ (e.g., [*Loewen and Melville*, 1994]), available evidence suggests that the V_0-*to*-E_D ratio (heretofore referred to as α)

varies across a narrow range for both types of breakers [*Long et al.*, 2011]. For example, measurements of V_0 and E_D for 2-D plunging breakers [*Lamarre and Melville*, 1991] yield α values of 5.6 (± 0.2) x 10^{-4} m^3 J^{-1} (n = 3) whereas measurements for both 2-D plunging and spilling breakers reported by *Blenkinsopp and Chaplin* [2007] yield α values of 2.2 (± 0.2) x 10^{-4} m^3 J^{-1} (n ≈ 10^3). Here, as in *Long et al.* [2011] we use an α value of 4.0 x 10^{-4} m^3 J^{-1}.

The air detrainment flux resulting from wave breaking (F_{Det} in m s^{-1}) can be estimated from [*Long et al.*, 2011]

$$F_{Det} = \alpha \varepsilon_d \quad (1)$$

where ε_d is the *rate* of energy dissipation by wave breaking (J m^{-2} s^{-1}) simulated with WWIII as described in more detail below.

Measurements of size-resolved PMA production efficiency, defined as the size-resolved particle yield per unit volume of air detrained from the water column (PE_{Num} in units of m^{-3}, [*Long et al.*, 2014b]) allow the PMA number production flux (F_{Num} in units of m^{-2}) to be calculated from F_{Det}:

$$F_{Num} = PE_{Num} \cdot \alpha \varepsilon_d \quad (2)$$

Currently in CAM, emissions of PMA with dry diameters (D_p) smaller than 2.8μm are based on the parameterization of [*Mårtensson et al.*, 2003] and those for larger particles are based on *Monahan* et al. [1986] as described by *Liu et al.* [2012]. The number flux for particles with dry diameters of 2.8 μm or smaller is in the form $dF_{Num}/dLogD_p$ (units of m_{oc}^{-2} m_{wc}^{-2} s^{-1} where subscripts *oc* and *wc* refer to surface area of the ocean and corresponding surface area covered by whitecaps, respectively) scaled with the wind-speed-dependent (U_{10} at 10 m height in m s^{-1}) white-cap area function of *Monahan and O'Muircheartaigh* [1986]. Although not reported in the literature, PMA emissions based on the default parameterization in CAM as summarized above are increased by a constant scaling factor of 1.35 to better fit cloud droplet number concentrations measured in the marine atmosphere (A. Gettleman, pers. comm., 2014).

Because the energy of wave breaking and associated air detrainment is a function of interactions between both wind and wave fields [*Tolman and Chalikov*, 1996], we hypothesize that sea state rather than wind velocity alone is the primary driver for PMA production. In the ambient environment, many wave properties are not in equilibrium

with associated wind fields due to temporal lags in wave response to changes in wind speed or direction. Unlike simplified scaling based on wind speed, prognostic wave models are able to simulate such non-equilibrium conditions. Wave breaking and associated PMA production are highly nonlinear processes that are sensitive to wave disequilibria [*Hanley et al.*, 2010; *Webb and Fox-Kemper*, 2011; *Cavaleri et al.*, 2012; *Edson et al.*, 2013]. Consequently, wave fields must be considered explicitly to reliably simulate PMA emissions.

To evaluate the influence of sea state, PMA emissions were simulated using four different production parameterizations as summarized below (details regarding the latter three approaches are described in subsequent subsections):

1) CAM's standard default parameterization driven by U_{10} and based on *Mårtensson et al.* [2003] and *Monahan et al.*, [1986] as described above (hereafter referred to as STD-U_{10}). Results using this parameterization represent the base case.
2) A wind-wave parameterization based on equation (1) and (2) using size-resolved PE_{Num} values measured by *Long et al.* [2014b] (hereafter referred to as WAVE).
3) A hybrid version of CAM'S default parameterization for which the wind-driven whitecap fraction was replaced with a wind-wave mechanism based on equation (1) and (2) and scaled to generate approximately the same integrated global PMA mass production flux as that simulated with STD-U_{10}. Relative to those simulated with STD-U_{10}, PMA production fluxes in this simulation (hereafter referred to as STD-WAVE) varied spatially in response to sea state rather than wind velocity alone.
4) To evaluate the influence of temperature on PMA production, a modified version of STD-WAVE was run for which the SST term in the PMA emission function was held constant at 291K (hereafter referred to as STD-$WAVE_{291K}$).

2.2.1 WAVE

The size-resolved particle number flux can be estimated directly from the wave field via a function of the form

$$\frac{dF}{dLogD_P} = F_{Det} \cdot \frac{dPE_{Num}}{dLogD_P} \quad (3)$$

where

$$\frac{dPE_{Num}}{dLogD_P} = 10^{P_N} \quad (4)$$

and P_N are polynomials fit to the size-resolved PE_{Num} values reported by Long et al. [2014b] for two aerosol size modes, *N*. Mode-1 corresponds to particles in the size range $0.01 < D_p < 0.4$ μm, and mode-2 corresponds to particles in the range $0.04 \leq D_p < 14$ μm. *Long et al*. [2014b] reported PE_{Num} values for PMA produced from both biologically productive and oligotrophic seawater and for bubble plumes generated with either a bank of fine porosity frits (10- to 20-μm pore size) or a coarse porosity frit (145- to 147-μm pore size). Since about 90% of the surface ocean is oligotrophic, the data used in this analysis correspond to those reported for oligotrophic conditions and, thus, we infer represent lower limits. PE_{Num} values for bubbles produced with fine frits were similar but not identical to those produced with the coarse frit [*Long et al.*, 2014b]. For consistency with past results reported for this generator, this analysis utilized data corresponding to the fine frits. For mode-1 and mode-2 particles, respectively,

$$P_1 = -0.28 \cdot logD_P^3 - 3.73 \cdot logD_P^2 - 7.31 \cdot logD_P + 6.59 \quad (5)$$

and

$$P_2 = -2.21 \cdot logD_P^3 - 1.4x10^{-2} \cdot logD_P^2 - 0.85 \cdot logD_P + 8.95 \quad (6)$$

2.2.1. STD-WAVE

Differences between size-resolved PMA production fluxes simulated with STD-U_{10} versus WAVE originate from two primary sources: (1) Differences between the relative shapes of PMA size distributions produced by a comparable set of physical drivers and (2) differences between the PMA produced as a function of wind speed versus sea state. To normalize for the influence of differences in the shape of the PMA size distribution and thereby enable direct comparisons between results based on wind speed alone (STD-U_{10}) versus the wind-wave approach, a hybrid parameterization was employed. The shape of the size distribution based on the default STD-U_{10} parameterization was adapted to utilize a wind-wave forcing in place of the wind-driven white-cap fraction. The parameterization for size-resolved number flux in STD-U_{10} is

$$\frac{dF}{dLogD_P} = W\Phi \quad (7)$$

where W is the white-cap fraction based on

$$W = 3.84 \times 10^{-4} U_{10}^{3.41} \quad (8)$$

from *Monahan and O'Muircheartaigh* [1986] and Φ is size-resolved, SST-dependent number production flux per whitecap fraction (m^{-2}). Our revised approach converts the whitecap fraction (*W)* in equation (7) to an air detrainment rate per equation (2) using a conversion factor C_F, which represents the ratio of whitecap-area dependence to air detrainment. C_F was calculated as

$$C_F = A_b \cdot R_{Det}^{-1} \quad (9)$$

where A_b (m^2) is whitecap area per *Mårtensson et al.* [2003] and R_{Det} ($m^3\ s^{-1}$) is the air volume detrainment rate. *Mårtensson et al.* [2003] report values for A_b and R_{Det} of 3.0173 x 10^{-4} m^2 and 1.67x10^{-7} $m^3\ s^{-1}$, respectively, which yields a C_F of 1810 s m^{-1}. As described in detail below (see Section 3.1), available evidence indicates that the value of C_F calculated directly from data reported by *Mårtensson et al.* [2003] is too high by a factor of approximately 13. It was necessary to scale C_F accordingly to yield production fluxes for STD-WAVE that were consistent with those based on the default *Mårtensson et al.* [2003] parameterization in STD-U_{10}.

For particles larger than 2.8-µm dry diameter, CAM employs the source function of [*Monahan et al.*, 1986], which scales directly with U_{10} rather than a U_{10}-driven white-cap fraction. Thus, the conversion factor used for emissions of PMA smaller than 2.8-µm diameter cannot be used to parameterize production of larger particles. For consistency, and in order to permit emissions for this portion of size range to be scaled as a function of ε_d, U_{10} was estimated based on *Hanson and Phillips* [1999] yielding

$$U_{10,Est.} \approx (2.34x10^4 \varepsilon_d)^{0.2674} \quad (10)$$

and thereby permitting direct scaling across the entire size distribution based on ε_d.

The final forms of the PMA emissions functions are,

$$\frac{dF}{dLogD_P} = C_F \cdot \alpha \varepsilon_d \Phi \quad (11)$$

for particles with dry diameters ranging from 0.1- to 2.8-µm, and

$$\frac{dF}{dr} = 1.373 U_{10,Est}^{3.41} r^{-3} (1 - 0.057 r^{1.05}) \cdot 10^{1.19 e^{-B^2}} \quad (12)$$

for particles larger than 2.8-μm dry diameter. In equation (12), r is the particle radius at 80% RH, and $B = (0.380 - Log(r))/0.650$.

2.2.3. STD-WAVE$_{291K}$

The *Mårtensson et al.* [2003] source function includes a sea-surface temperature dependence in equation (9) where $\Phi = A \cdot SST + B$, A and B are size-resolved regression parameters, and SST is in Kelvin. Evidence based on model calculations using offline meteorology also suggest a SST dependence in PMA production [*Jaeglé et al.*, 2011; *Grythe et al.*, 2014], albeit different from that that reported by *Mårtensson et al.* [2003]. To evaluate the temperature dependence of PMA emissions in STD-WAVE, aerosol production was simulated using an alternate version of the wave parameterization in which SST was held constant at 291K, the average temperature for the NOAA Reynolds SST climatology [*Reynolds et al.*, 2002, 2007]. Temperature was held constant only for the calculation of PMA. Temperature dependence of the simulation of atmospheric boundary layer stability or the air-sea momentum coupling was not modified.

The PMA flux parameterization for WAVE evaluated the dry-particle diameter range of 0.013 to 14 μm whereas those for STD-U_{10}, STD-WAVE and STD-WAVE$_{291K}$ evaluated the range 0.02 to 11.4 μm. However, the CAM PMA emission routine integrates the particle source flux across dry diameters ranging from 0.2 μm to 10 μm into three lognormal modes specified below (Section 2.4). Thus, differences in the ranges of particles sizes evaluated by these PMA production parameterizations did not impact results.

2.3 Calculation of Wave Breaking Energy

The energy dissipation rate ε_d was estimated at every wave model grid point from the wave model output of the wave variance spectrum, $\psi(k,\theta)$. ε_d can be estimated by directly integrating the wave energy loss term evaluated by the wave model. However, at the time of the model runs reported herein, the wave energy loss term was not a standard model output. For this work, ε_d was estimated as described below based on the simulated flux of energy from wind into waves, $\tilde{F}_W$, (kg s^{-3}) and the energy taken up or released by the waves. Wave energy loss was subsequently added as a standard output of the most recent

version of WWIII and an as yet unpublished comparison of simulated versus independently calculated loss terms revealed very good agreement [B. Reichl and T. Hara, unpublished results].

The flux of energy from the wind into the waves can be calculated from the wave growth rate, $\beta_g(k,\theta)$ (s^{-1}), and the wave variance spectrum, $\psi(k,\theta)$:

$$\tilde{F}_W = \int_{-\pi}^{\pi}\int_0^{\infty} \beta_g(k,\theta)\rho_W g\Psi(k,\theta)k\, dk\, d\theta, \quad (13)$$

where $\beta_g(k,\theta)$ is specified (e.g., [*Hara and Belcher*, 2004]) as

$$\beta_g(k,\theta) = c_\beta \sigma \frac{\rho_a u_*^2}{\rho_w c^2}\cos^2(\theta-\theta_{wind}) \quad (14)$$

and the non-dimensional growth rate coefficient is

$$c_\beta = 32 \qquad \text{if } \cos(\theta-\theta_{wind}) > 0 \text{ and } u_*/c > 0.07,$$

$$c_\beta = 0 \qquad \text{otherwise.}$$

k is the wavenumber (m^{-1}), θ is the wave direction (radians), ρ_W and ρ_a are the water and air density, respectively (kg m^{-3}), g is acceleration by gravity (m s^{-2}), $\sigma = \sqrt{gk}$ is the angular frequency, $c = \sigma/k$ is the wave phase speed (m s^{-1}), θ_{wind} is the wind direction (radians), and u_*^2 is the air-side friction velocity in the wave model ($u_*^2 = \tau/\rho_a$ in units of m^2 s^2 and τ is the wind stress).

The energy contained within the surface wave field (E in units of J) is calculated from the spectrum:

$$E = \int_{-\pi}^{\pi}\int_0^{\infty} \rho_W g\Psi(k,\theta)k\, dk\, d\theta, \quad (15)$$

and the horizontal energy fluxes (in x and y directions) due to wave propagation are calculated as:

$$EF_x = \int_{-\pi}^{\pi}\int_0^{\infty} \rho_W g C_g\Psi(k,\theta)\cos(\theta)\, k\, dk\, d\theta, \quad (16)$$

$$EF_y = \int_{-\pi}^{\pi}\int_0^{\infty} \rho_W g C_g\Psi(k,\theta)\sin(\theta)\, k\, dk\, d\theta, \quad (17)$$

where C_g is the group velocity ($c/2$ in m s^{-1}). The energy dissipation rate (ε_d) can then be calculated as the energy input from air minus the energy taken up by the waves (the horizontal divergence of the wave energy flux and the time rate of change (growth or decay) of the wave energy):

$$\varepsilon_d = \tilde{F}_W - \left(\frac{\partial EF_x}{\partial x} + \frac{\partial EF_y}{\partial y}\right) - \frac{\partial E}{\partial t}. \quad (18)$$

Contributions from waves with frequencies less than 3 x f_π where f_π is the wind-wave peak frequency are not resolved by the wave model but are negligibly small [*Fan et al.*, 2010].

2.4 Modeled AOD

Details of the aerosol microphysical scheme and calculation of aerosol optical properties are reported by *Ghan and Zaveri* [2007] and *Liu et al.* [2012]. Briefly, for simulations reported herein, CAM explicitly calculated number and mass moments of three log-normally distributed size modes equivalent to Aitken, accumulation, and coarse aerosol size ranges centered log-normally on 0.026-, 0.11-, and 2.0-μm geometric mean dry diameters (GMD), respectively. Corresponding lognormal standard deviations were 1.6, 1.8, and 1.8, respectively, and the corresponding ranges were 0.0087-to-0.052-, 0.053-to-0.44-, and 1.0-to-4.0-μm dry diameter, respectively. Each mode is comprised of an internal mixture of non-sea-salt (nss) sulfate, OM from primary sources, secondary OM from condensation of volatile organic precursors, black carbon, inorganic sea salt, and mineral dust. AOD in CAM is calculated based on *Ghan and Zaveri* [2007] and varies as a function of deliquesced particle size, area density, volume-weighted mean hygroscopicity of internally mixed aerosol, and relative humidity (RH). Hygroscopic growth factors are set to 0.507, 0.10, 0.14, $1x10^{-10}$, 1.16, and 0.068 for nss sulfate, primary OM, secondary OM, black carbon, sea salt, and dust, respectively.

2.5 Simulations

All results reported herein correspond to simulations at a horizontal resolution of 0.9^o x 1.25^o latitude/longitude for the ocean, atmosphere, wave, and land component grids (including land ice), and a 1^o displaced-pole grid (GX1v6) for the ocean. CAM was configured with CAM5 physics options using the finite volume dynamical core and the 3-mdre aerosol module [*Liu et al.*, 2012]. Each simulation was run for 6 years including one year for atmospheric equilibrium. Statistical analysis was performed on the final five simulation years. All simulations were performed on the Oak Ridge National Laboratory – Oak Ridge Leadership Computing Facility's Titan Cray XK7 system.

2.5 Observational Data

2.5.1 Sea-Surface Temperature

SST used for both boundary conditions for CAM within the CESM and for data analysis were derived from the Reynolds climatology [*Reynolds et al.*, 2002, 2007]. These data were derived from a series of interpolated global analysis products in 1° and ¼° grid horizontal grids, followed by regridding to the horizontal resolution used in simulations here.

2.5.2 Particulate Na^+ Concentrations

Mean simulated concentrations of bulk particulate Na^+ in the lowest level of the model were compared with corresponding mean concentrations of bulk particulate Na^+ measured in near-surface marine air at 19 sampling stations operated over multi-year periods under the auspices of the Atmosphere/Ocean Chemistry Experiment (AEROCE), Sea-Air Exchange (SEAREX), and the U.S. Department of Energy Environmental Monitoring Laboratory (DOE-EML) programs [*Savoie and Prospero*, 1977; *Galloway et al.*, 1993; *Dentener et al.*, 2006; *Textor et al.*, 2006]. These observations provide broad geographic coverage ranging from 63.4N to 67.6S latitude.

2.5.3 Aerosol Optical Depth (AOD)

AOD data evaluated herein are from the newly released Collection 6 (C6) over ocean Aqua MODIS Dark Target (DT) aerosol product [*Levy et al.*, 2013]. Uncertainties and sporadic positive biases due to cloud contamination and whitecaps exist in the standard C6 over ocean DT aerosol products [*Shi et al.*, 2014]. Consequently, we applied additional quality assurance methods similar to those used in constructing data assimilation grade Collection 5 MODIS DT aerosol products [e.g., Shi et al., 2011]. To minimize cloud contamination, retrievals with cloud fractions greater than 20% and retrievals with average distances to clouds of less than 2 pixels (as determined from the Cloud_Pixel_Distance_Land_Ocean parameter) were excluded. Buddy checks and a bias correction for lower boundary conditions based on operational wind speed data (similar to that described by *Shi et al.* [2011, 2014] were also applied to further reduce uncertainties and biases.

Only conditions dominated by marine aerosol (clean marine regions) are relevant to this study. However, some regions over the global oceans often contain high concentrations of aerosols from continental sources such as combustion-derived and mineral aerosol transported from eastern Asia over the western North Pacific Ocean and from North Africa over the tropical North Atlantic Ocean. The Navy Aerosol Analysis and Prediction System (NAAPS) reanalysis (Peng et al., Development Studies Towards a 11-year Global Gridded Aerosol Optical Thickness Reanalysis for Climate and Applied Applications, 2015, in preparation) was used to differentiate between AOD observations that were dominated by aerosol from marine versus continental sources. NAAPS is a chemical transport modeling system that provides 6-day aerosol forecasts for the US Navy operationally (http://www.nrlmry.navy.mil/aerosol/). The NAAPS reanalysis is generated with an offline version of NAAPS that simulates contributions of sea salt, dust, smoke, and anthropogenic and biogenic fine particles (ABF) to AOD at 1x1° (Latitude/Longitude) resolution every 6 hours from 2003-2013. The NAAPS analysis, which is available from the GODAE server (http://www.usgodae.org/docs/naaps-reanalysis.html), is generated through assimilation of quality assured Collection 5 MODIS DT and Multi-angle Imaging SpectroRadiometer (MISR) AOD data [*Zhang et al.*, 2008, 2014; *Hyer et al.*, 2011; *Shi et al.*, 2011].

Four steps were applied to the C6 MODIS AOD data to identify the subset of retrievals that were dominated by marine aerosol and to construct the level 3 AOD data used in this analysis. 1) MODIS retrievals with AOD less than 0.07 (at 0.55 μm) were retained as these retrievals are within the baseline oceanic AOD value suggested by *Kaufman et al.*, [2002]. 2) Retrievals with AODs greater than 0.3 were assumed to be dominated by non-marine aerosol and, thus, excluded. 3) For retrievals with AODs between 0.07 and 0.3, ratios of column-integrated contributions of sea-salt AOD to total AOD ($R_{seasalt}$) were computed from the collocated NAAPS data. Only retrievals with $R_{seasalt}$ greater than or equal to 0.5 were assumed to be dominated by marine aerosol and, thus, retained. Based on C6 MODIS AOD retrievals filtered as described above, monthly-averaged AODs were constructed at a 1x1° (Latitude/Longitude) spatial resolution for the period of July 2002 to December 2006.

For comparison to model output, only AOD in grid cells with $U_{10} \geq 6$ m s^{-1} were used. Further, MODIS AOD at high latitudes is limited to spring and summer periods, warranting caution when interpreting model versus observed AOD.

2.5.4 RH and Surface Wind

RH and surface wind data for use in model comparison and validation were based on the NCEP/NCAR Reanalysis 1 project long term monthly means datasets derived from data for years 1981 – 2010 [*Kalnay et al.*, 1996] available from http://www.esrl.noaa.gov/psd/data/gridded/data.ncep.reanalysis.html.

3. Results and Discussion

3.1 Size-Resolved PMA Production Fluxes

The size-resolved PMA source functions were evaluated for consistency prior to running within the full CESM. Size-resolved production based on STD-U_{10} at U_{10} = 9 m s^{-1} and SST = 298K was compared to that based on WAVE at an equivalent F_{Det} calculated as per Long et al. [2011] ($F_{Det} = 2 \times 10^{-8}\ U_{10}^{3.74}$). Both functions yielded similar results (Figure 1a). Production based STD-WAVE per equation (11) was compared to WAVE at $\varepsilon_d = 0.16$ J m^{-2} s^{-1}, which is equivalent to $U_{10} \approx 9$ m s^{-1} per on equation (10), and $F_{Det} = 6.4 \times 10^{-5}$ m s^{-1} per Long et al. [2011]. It is evident from Figure 2 that equation (10) provides a reasonable approximation of U_{10} based on ε_d calculated online with WWIII. For D_P less than 2.8 µm, the production function in STD-WAVE (equation 11) yields size-resolved PMA fluxes that are more than an order of magnitude greater than those based on STD-U_{10} and WAVE (Figure 1b).

The likely cause for this large discrepancy is that C_F calculated from equation 9 is substantially overestimated. For D_P less than 2.8 µm, the relative shapes of PMA production as functions of particles size are similar (Figure 1), which strongly suggests that (1) whitecap area and energy dissipation are directly related and (2) the empirical relationships between W and ε_d versus U_{10} (per *Monahan and O'Muircheartaigh* [1986] and *Hanson and Phillips*, [1999], respectively) permit reasonable and interchangeable approximations. These results also imply that PE reported by *Long et al.* [2014b] and the estimation of α in *Long et al.* [2011] yield reasonable approximations of particle

475 production relative to other PMA source functions. For D_P less than 2.8 µm, the
476 consistency between size-resolved production based on STD-U_{10} and WAVE (Figure 1a)
477 coupled with the results presented in *Mårtensson et al.* [2003], suggests that the
478 conversion of PMA flux as a function of W to flux as a function of ε_d using C_F is the
479 cause for the high PMA flux for STD-WAVE depicted in Figure 1b.
480 Per equation (9), C_F is based upon the air detrainment rate, R_{Det}, and the corresponding
481 surface area covered with bubbles, A_b (equivalent to whitecap area). We assumed that the
482 measurement of the air detrainment rate is accurately reported by *Mårtensson et al.*,
483 [2003]. However, the measurement of A_b was probably associated with greater
484 uncertainty and the authors do not describe the corresponding methodology. Assuming
485 that Figure 1 confirms the relationships between W and ε_d versus U_{10}, we estimate that a
486 whitecap area between 4 x 10^{-3} and 5 x 10^{-3} m^2 would be generated at the reported air
487 detrainment rate of 10 mL min^{-1} (1.67 x 10^{-7} m^3 m^{-2} s^{-1}), which is equivalent to that at a
488 U_{10} of approximately 2 m s^{-1}. This value for A_b differs from that in *Mårtensson et al.*,
489 [2003] by a factor of approximately 0.075. When production of particles with D_P less
490 than 2.8 µm in STD-WAVE were scaled by 0.075, the resulting size-resolved PMA flux
491 was in far better agreement with those based on STD-U_{10} and WAVE (Figure 1b). We
492 conclude that the A_b reported in *Mårtensson et al.* [2003] may be incorrect. We note that
493 the units for A_b reported by *Mårtensson et al.* [2003] are also incorrect; m^{-2} should be m^2.
494 Based on the above, for D_P less than 2.8 µm STD-WAVE and STD-$WAVE_{291K}$, C_F in
495 equation (11) was scaled by 0.075 yielding an adjusted C_F value of 135.8 s m^{-1}.
496
497 3.2 U_{10} vs. ε_d
498 The wave-energy dissipation fluxes simulated by WWIII for the major ocean basins
499 were generally greater (mean factor of 2.3 ± 2.0) than those predicted by *Hanson and*
500 *Phillips* [1999] based on U_{10} alone (Figure 2), though are well within the range of scatter
501 of their observations (statistics were not reported). In mid- to high-latitude regions with
502 climatologically higher wind velocities and more developed and energetic wave fields,
503 the simulated wave dissipation fluxes were systematically greater. The relative
504 differences are most evident for the North Pacific and North Atlantic Oceans above 30°N
505 (Figure 2a and c, blue and pale green markers, respectively), and the high-latitude

Southern Ocean south of 30°S (Figure 2d). In the vicinity of the Pacific and Atlantic gyres (Figure 2a and c, green and olive markers, respectively), simulated ε_d was only slightly higher (factors of 1.4 ± 0.7 and 1.1 ± 0.1, respectively) than that based on [*Hanson and Phillips*, 1999] and overlaps the observed ε_d vs. U_{10} estimated by [*Felizardo and Melville*, 1995] (not shown).

The systematic offset between simulated ε_d relative to that predicted based on *Hanson and Phillips* [1999] (Figure 2, black lines) in the high-latitude Pacific and Atlantic basins versus gyre regions implies fundamental differences in relationships among wind velocity, wave fields, and energy dissipation in high- versus low-latitude regions. Differences in the magnitudes of the offsets between mid and high-latitude ε_d fields in the Pacific and Atlantic Oceans (Figure 2a and c) and the relatively high ε_d / U_{10} ratio in the Southern Ocean (Figure 2d) suggest more efficient transfer of wave energy into the dissipation term in high-latitude wave fields. It is evident from equation (2) that this more efficient transfer would in turn drive relatively greater PMA emissions per unit wind velocity at higher latitudes. Consequently, relative to those scaled from ε_d, PMA production fluxes scaled directly from U_{10} also diverge systematically among major oceanic regions.

3.3 STD-U_{10} versus WAVE

Relative to WAVE, number production fluxes simulated with STD-U_{10} were lower in tropical oceanic regions but moderately higher in the high-latitude southern ocean (Figure 3). Integrated globally, the mean number production flux simulated with WAVE was higher by a factor of 1.3 (Table 1). In contrast, the corresponding global mass flux based on WAVE was lower by a factor of 2.3. As indicated in Section 2.2.1, these differences are driven primarily by two factors: (1) the shape of the size-resolved PMA production distribution and (2) variability in PMA produced as a function of U_{10} versus ε_d. This is consistent with the relative differences between PMA production based on STD-U_{10}, STD-WAVE, and WAVE size distributions as depicted in Figure 1.

Relative shapes of measured production distributions for size-resolved PMA vary in response to numerous factors including the mechanisms by which bubble plumes were produced (frits, jets, and waves tanks, and associate variability in air detrainment rates

and bubble-plume dynamics), the types of solutions from which PMA were produced (natural open-ocean seawater in biologically productive versus oligotrophic regions and associated time of day, coastal seawater, artificial seawater, seawater amended with organic surfactants), and temperature [e.g., *Mårtensson et al.*, 2003; *Hultin et al.*, 2010, *Long et al.*, 2011, 2014; *Prather et al.*, 2013]. Some parameterizations (including STD-U_{10}) consider poorly constrained contributions from spume droplets whereas others (including WAVE) do not, which contributes to relatively higher mass fluxes in the former [*Long et al.*, 2011]. A related source of variability in simulated mass flux based on different parameterizations involves to the upper size cutoff for the production distribution [e.g., *Lewis and Schwartz*, 2004; *Andrea and Rosenfeld*, 2008]. With increasing cutoff size, relative contributions from very coarse but short-lived particles increase thereby driving greater integrated mass fluxes for given sets of condition. A detailed evaluation of variability in number and mass production fluxes introduced by differences in the shape PMA size distribution is beyond the scope of this study. The primary focus of this effort is to differentiate relative influences of wind speed versus sea state on number and mass production fluxes of PMA. As described above, to evaluate this source of variability, we developed the hybrid parameterization (STD-WAVE), which adopted the shape of the production parameterization in STD-U_{10} but replaced the U_{10} driver with an energy dissipation function, which yielded approximately the same integrated global mass flux of PMA. This approach allowed spatial variability in PMA production fluxes for the two simulations to be evaluated based on differential influences of the U_{10} versus ε_d drivers.

3.4 STD-U_{10} versus STD-WAVE

The integrated global mass fluxes of PMA simulated with STD-U_{10} and STD-WAVE were nearly identical (Table 1). However, significant geographic differences were evident in both mass fluxes and burdens (Figure 4 and 5, respectively). Two important features stand out: 1) The zonal band of high aerosol mass flux in the mid and high-latitude southern ocean was much less pronounced in the STD-WAVE results (Figure 4b) whereas (2) the corresponding number fluxes tended to be greater (Figure 4a). Similarly, the STD-WAVE PMA mass concentration in the atmospheric surface layer of the high-

latitude southern hemisphere (Figure 5b) lacks the distinctive zonal maximum band evident in the STD-U_{10} results (Figure 5a), and the overall mass concentration distribution reflects the latitudinal variability in the aerosol production flux (Figure 4).

In contrast to the good agreement between globally integrated mass fluxes in the two simulations, number fluxes differed by a factor of 1.4 (Table 1). The primary cause for this divergence was relatively greater number production fluxes simulated by STD-WAVE in near-coastal regions where fetch-limitation and sea ice are prevalent, and influences of bathymetry and wind-wave field interaction impact ε_d (Figure 3f).

3.5 STD-WAVE versus STD-WAVE$_{291K}$

Relative to STD-WAVE, STD-WAVE$_{291K}$ yielded lower integrated number and mass production fluxes of PMA (Table 1). These differences reflect the SST dependence of size-resolved PMA production in STD-WAVE as originally formulated by *Mårtensson et al* [2003] (equation 7). For a given wind velocity in STD-WAVE, relative production of smaller particles decreases and relative production of larger particles increases with increasing temperature. These temperature-dependent relationships were evident in relative differences in latitudinal variability for number and mass production fluxes simulated based on the two parameterizations (Figure 6). Compared to STD-WAVE, STD-WAVE$_{291K}$ yields proportionately higher number fluxes and proportionately lower mass fluxes in lower, warmer latitudes and visa-versa in higher, colder latitudes.

3.6 Comparison to Observation

3.6.1 Observed Atmospheric Na^+ Concentrations

Na^+ concentrations in the lowest model layer simulated with STD-U_{10} and STD-WAVE were weakly correlated with average Na^+ concentrations measured in near-surface marine air but results indicate substantial scatter (Figure 7). In addition, ratios of simulated to observed Na^+ for the two parameterizations tended to increase with increasing U_{10} greater than about 8 m s^{-1}. Removing the SST dependence in STD-WAVE$_{291K}$ did not significantly improve the comparison to observations relative to STD-U_{10} ($p>0.2$) (Figure 7).

598 Unpublished tests by the University of Miami (D. Savoie and M. Izaguirre, personal
599 communication, 2013) indicate collection efficiencies ranging from 85% to ~100% for
600 particulate Na^+ and other particulate-phase species suggesting that Na^+ concentrations
601 associated with the long-term datasets reported by the University of Miami should be
602 reasonably representative of those in ambient air. However, physical relationships
603 indicate that inertial segregation of larger particles at inlets may cause negative sampling
604 bias at higher wind velocities. Such effects may have contributed to the systematic
605 divergence between simulated versus measured concentrations at higher wind speeds
606 (Figure 7).
607 Other factors such as uncertainties associated with aerosol physics and wind fields
608 within the CAM atmosphere likely contribute to these differences. For example, mass-
609 median diameters for ambient marine aerosol size distributions tended to increase with
610 increasing mass concentration [e.g., *Keene et al., 2009*]. Because larger particles exhibit
611 relatively higher dry-deposition velocities and associated shorter lifetimes against
612 deposition [e.g., *Hummelshøj et al., 1992*], disproportionately greater production fluxes
613 of larger particles would be required to sustain higher mass median diameters, which
614 implies that mass-integrated atmospheric lifetimes of marine aerosols tend to decrease
615 with increasing mass. However, in CAM, super-um diameter size fractions, which
616 dominate marine aerosol mass, are binned into a single log-normally distributed size
617 mode centered on 2.0 μm dry GMD. Because the relative shape and geometry of the
618 coarse-mode marine aerosol distribution in CAM does not vary as a function of mass, it
619 follows that simulated dry-deposition fluxes at higher wind velocities may underestimate
620 ambient dry-deposition fluxes. Consequently, the corresponding simulated mass
621 concentrations may overestimate ambient concentrations, consistent with the divergence
622 between simulated versus measured Na^+ concentrations at higher wind velocities evident
623 in Figure 7.
624
625 3.6.2 Comparison to Observed AOD
626 Regional differences between modeled versus remotely-sensed AOD (Figure 8) reflect
627 numerous factors in addition to those associated directly with the calculation of AOD in
628 the model. For example, widespread cloud cover over high-latitude regions during winter

limits the availability of AOD measurements. Consequently, annual average AODs at higher latitudes are weighted disproportionately by measurement during warmer months when wind speeds, sea states, and PMA production are typically lower. However, annual averages based on simulated AODs are weighted equally by all seasons. Consequently, the absence of AOD observations for the higher-wind season would introduce negative bias in annual average values. Negative bias in AOD may also occur under clear sky conditions [*Zhang and Reid*, 2009]. Conversely, other sources of biases in AOD retrievals are largely positive (e.g., cloud contamination, whitecap error, etc.). While the filters applied to assimilation-grade data minimize such sources of bias, they do not fully eliminate them. Finally, aerosols in marine air are never comprised exclusively of one aerosol type, which constrains the reliability of direct comparisons between simulated and observed AOD. It is evident that annual average AOD based on observations, particularly at higher latitudes, may not be entirely representative of annual average AOD in the ambient atmosphere and, thus, should be interpreted with caution and an appreciation of associated limitations. Nevertheless, observed AOD provides a useful benchmark against which model performance can be evaluated.

As discussed in Section 3.6.1, the binning of most marine aerosol mass into a single size mode may introduce positive bias in the simulated aerosol burden and associated AOD at higher wind velocities. In addition, differences between modeled and ambient wind patterns, boundary layer structure, and aerosol populations also constrain the reliability of direct comparisons. For example, in some regions, differences between modeled and observed AOD varied in response to the corresponding positions and size of major synoptic circulation features. Large positive deviations in AOD simulated with both STD-U_{10} and STD- WAVE (Figure 8a and b) relative to observed AOD (Figure 8c) over the eastern South Pacific and southern Indian Oceans, and a large zonal negative deviation over the higher-latitude southern ocean adjacent to Antarctica suggests that CAM was unable to accurately predict wind and wave fields and the corresponding marine-aerosol burdens in these regions.

Inaccurate RH, aerosol hygrosocopity, and mixed layer structure within the model may also introduce bias. Relative to MODIS-C6 AOD, simulations based on STD-U_{10}, STD-WAVE, and STD-$WAVE_{291K}$ overestimated AOD over the northern hemisphere

oceans by median factors of 25±42%, 22±40% and 44±33% respectively. As noted previously, a scale factor of 1.35 is applied to PMA production in CAM to correct for systematic divergence between simulated versus observed cloud droplet number concentrations in marine regions. If this scale factor were removed, global mean biases between simulated and observed AOD would decrease to -7.7±31%, -9.8±29% and 6.5±24% for the STD-U_{10}, STD-WAVE, and STD-$WAVE_{291K}$ results, respectively.

While this bulk comparison suggests that the use of the standard 1.35 scale factor may have contributed to systematic positive bias in simulated AOD, such a result can easily be over-interpreted. The standard error in AOD over oceanic regions that are dominated by marine aerosol (e.g. the southern ocean) is on the order of ±50% [*Shi et al.*, 2011]. No discernible relationship between AOD deviations and RH biases were evident (Figure 8 and 9; Also see Figure S2). Relative to NCEP Reanalysis data from 2002-2006, CAM systematically underestimated mid-latitude RH at the surface and overestimated RH at 850 hPa (Figure 9), though the NCEP reanalysis is known to have significant regional biases as well [*Vey et al.*, 2009]. This implies a vertical component to differences between modeled and observed AOD. Given the aerosol size modes in CAM, virtually all PMA would be mixed throughout the marine boundary layer. Thus, the net influence of uncertainty in RH on simulated AOD and associated comparison with observations is unclear.

3.7 Comparison to Surface Seawater State

3.7.1 SST Dependence

Several studies report evidence of a direct link between rates of marine aerosol production and sea-surface temperature. *Jaeglé et al.* [2011] report a weak but significant correlation between modeled and observed marine aerosol concentration differences and sea-surface temperature. Data from *Long et al.*, 2014b suggest a weak correlation between SST and daytime PE_{Num}, though it is not sustained during nighttime, and variable operating conditions constrain resolution in evaluating the effect. *Mårtensson et al*. [2003] also observed a size-resolved temperature dependence of the number production flux that was included in the STD-U_{10} and STD-WAVE parameterizations used here.

691 Figure 10 compares the ratio of modeled to observed marine-aerosol mass for STD-U_{10},
692 STD-WAVE, and STD-$WAVE_{291K}$ to the Reynolds SST climatology. The observations
693 correspond to those at the long-term sampling stations described in Section 2.5.2 that
694 were used both here and by *Jaeglé et al.* [2011]. Our simulations revealed no trends in
695 observed Na^+ concentrations relative to SST (Figure 10).
696 Differences between our results and those presented in *Jaeglé et al.* [2011] could be due
697 to differences in meteorology between our fully prognostic simulation and the offline
698 assimilated meteorology used by *Jaeglé et al.* [2011]. However, simple comparison
699 between 5-year mean surface wind speed from STD-U_{10} and the NCEP/NCAR reanalysis
700 long-term monthly climatological mean (covering 1981-2010; Figure S1) indicated no
701 significant difference between them. Standard linear regression yielded the line $y = 0.92x$
702 $+ 0.068$ ($r^2 = 0.79$; $p << 0.05$). The regression slope was significantly different than 1 (p
703 < 0.05); but a slope of 0.92 is within the cumulative uncertainty in observations of Na^+
704 [*Long et al.*, 2011]. Thus, we conclude that the difference between the our results and
705 those of *Jaeglé et al.* [2011] are due to factors other than differences in surface winds,
706 and are more likely due to large differences in processes controlling aerosol transport and
707 physics (e.g. see Liu et al. 2012 and http://www.geos-chem.org/#Aerosols).
708 Since simulated aerosol optical properties represent the cumulative result of modeled
709 aerosol processes, comparison of modeled to observed AOD as a function of SST can
710 reveal differences not captured by corresponding comparisons of aerosol mass. Several
711 relevant relationships are evident in Figure 11: (1) The inclusion of a wave-state based
712 Na^+ emission function in STD-WAVE did not modify the SST dependence in AOD
713 relative to that simulated by STD-U_{10} (Figure 11a,b,d). (2) Relative to STD-U_{10}, the STD-
714 $WAVE_{291K}$ simulation revealed a step-wise transition from a high to low bias iin Na^+
715 emission versus SST (Figure 11e). The step-wise change reflects the basin-scale
716 variability in the wind-wave field discussed in Section 3.2. (3) Relative to STD-U_{10}, the
717 wind-wave based parameterization in STD-WAVE had little discernible impact on the
718 SST dependences of the ratio between observed to simulated AOD (Figure 12a,b,d).
719 These relationships are consistent with similarities in distributions of AOD simulated by
720 STD-U_{10} and STD-WAVE (Figure 8) and, in particular, do not reflect the relatively
721 larger corresponding differences in spatial distributions of simulated PMA mass

722 production fluxes (Figure 4). As discussed above, these results suggest that factors other
723 than the PMA source function account for most of the divergence between observed and
724 simulated AOD. (4) Removing the SST dependence improved the agreement between
725 simulated vs. observed AOD (Figure 12c). The large model uncertainty associated with
726 convection and cloud processes at high SST (e.g. the tropics), and the combined
727 uncertainty in model RH and observed AOD at high latitudes discussed above constrain
728 unequivocal interpretation of these results. We infer that any apparent SST dependence in
729 simulated PMA production is small relative to other sources of uncertainty and may be an
730 artifact resulting from differences in aerosol treatment among model systems.
731
732 3.7.2 Chl-a dependence
733 Several studies have suggested links between PMA and biological activity in the
734 surface ocean that impacts the associated emission, composition, processing and optical
735 properties of aerosol. Most focus on the inferred influence of marine microbiology on the
736 partitioning of inorganic sea salt constituents and organic matter associated with size
737 resolved PMA based on weak or hypothetical correlations with remotely sensed Chl *a*
738 (e.g. [*Gantt et al.*, 2009; *Long et al.*, 2011; *Rinaldi et al.*, 2013; *Partanen et al.*, 2014]).
739 Others find no correlation with Chl-a [*Quinn et al.*, 2014] and a primary impact of
740 biological activity on total emission fluxes rather than on organic/inorganic fractionation
741 [e.g. *Long et al.*, 2014b]. It is reasonable to hypothesize that any impact of ocean biology
742 on PMA optical properties could be discerned by comparing AOD in the marine
743 atmosphere to our simulated results that do *not* include a biological effect. Comparing the
744 ratios of modeled to observed AOD and Na^+ mass concentration to average observed
745 Chl-a from 2002 to 2006 revealed no significant correlations (Figure 13). Ultimately,
746 while connections between some metric of surface ocean biology and PMA production
747 are clearly evident in laboratory and field studies, the signal is negligible relative to the
748 overall variability and uncertainty in the system [*Long et al.*, 2014b; *Quinn et al.*, 2014].
749
750 4. Summary and Conclusions
751 1) The offset between mid and high-latitude ε_B fields in the Pacific and Atlantic oceans
752 (Figure 2) reflects a more efficient transfer of wave energy into the dissipation term in

more highly developed wave fields, yielding relatively higher PMA emissions per unit wind velocity. These results imply that interactions among wind fields and wave fields must be considered explicitly to reliably simulate the corresponding PMA production.

2) Relative to results based on STD-U_{10}, the incorporation of a the coupled wind-wave parameterization in STD-WAVE did not significantly improve overall model performance against observed AOD or Na^+ concentrations.

3) Air entrainment rates simulated by WWIII were within ranges reported for wave tank studies and used for chamber and tank-based PMA production experiments. These results suggest that experimentally determined rates of PMA production per unit air detained can be reliably extrapolated based on the simulated air detrainment rates.

4) There was no discernible correlation between observed SST or Chl-a and observed or modeled AOD or Na^+ concentrations.

5) Ultimately, comparison of simulated results to observations relevant to PMA production and processing in the CESM underscored the uncertainty in the model physics. This uncertainty coupled with the combined uncertainty of the observations themselves constrain our ability to identify model improvement using an arguably more physically accurate description of the dominant global source for aerosol mass. The use of assimilated meteorology to minimize meteorological bias globally would likely eliminate sole of the uncertainty thereby facilitating more useful comparisons with observations. Still, this study has provided several advances, primarily,

    a. The use of a prognostic wave model to simulate wind-wave interactions reduces a major source of uncertainty in current parameterizations of PMA production thereby improving resolution in addressing other sources of uncertainty.

    b. Our results support for the efficacy and scalability of direct lab and field based observations of the primary physical processes controlling PMA production (e.g. *Lamarre and Melville, 1991; Keene et al., 2007, Blenkinsopp and Chapin, 2007; Long et al., 2014*).

5. Acknowledgements

784 Financial support was provided by the US Department of Energy's Office of Science
785 through the Office of Biological and Environmental Research (BER, grant number DE-
786 SC0007120 to the University of Virginia). Additional support was provided by the
787 National Science Foundation (awards OCE-1129836 and NSF-1258907) and NASA
788 (NNX09AF38G). NCEP Reanalysis Derived data provided by the NOAA/OAR/ESRL
789 PSD, Boulder, Colorado, USA, from their Web site at http://www.esrl.noaa.gov/psd/.
790 Data used for this manuscript is available upon request to the corresponding author.
791
792 6. Notation
793 A_b water surface area through which bubbles are bursting, m^2
794 c wave phase speed, $m\ s^{-1}$
795 c_β non-dimensional wave growth rate coefficient
796 CF whitecap area to PE conversion factor, $s\ m^{-1}$
797 C_g wave group velocity, $m\ s^{-1}$
798 D_p dry particle diameter, µm
799 E energy contained in the surface wind-wave field, J
800 E_D wave energy dissipated by breaking, J
801 F_{Det} bubble plume air detrainment flux, $m\ s^{-1}$
802 F_{Num} particle number flux, $m^{-2}\ s^{-1}$
803 F_T total particle number flux, $m^{-2}\ s^{-1}$
804 F_w energy flux from wind into the wave field, $J\ m^{-2}\ s^{-1}$
805 f_π wind-wave peak frequency, s^{-1}
806 g accelleration gue to gravity, $m\ s^{-2}$
807 k wave number, m^{-1}
808 PE_{Num} PMA number production efficiency per unit bubble volume, m^{-3}
809 P_N regression polynomial for particle mode n.
810 r particle radius at 80% RH
811 R_{Det} bubble plume air detrainment rate, $m^3\ s^{-1}$
812 RH relative humidity
813 u_* wind friction velocity, $m\ s^{-1}$
814 U_{10} wind speed at 10 meters above the surface, $m\ s^{-1}$

815 V_0 volume of air entrained by a breaking wave, m^3

816 W whitecap fraction

817 α ratio of air entrained per unit energy dissipated by wave breaking

818 β_g wave growth rate, s^{-1}

819 ε_d wave energy dissipation flux, J m^{-2} s^{-1}

820 θ wave direction, radians

821 Φ size-resolved number production flux per unit whitecap area, m^{-2} s^{-1}

822 ψ wave variance spectrum

823 ρ_w density of seawater, kg m^{-3}

824 ρ_a density of air, kg m^{-3}

825 σ angular frequency, s^{-1}

826 τ wind stress, Pa

827

828 7. References

829 Blenkinsopp, C. E., and J. R. Chaplin (2007), Void fraction measurements in breaking
830 waves, *Proc. R. Soc. Math. Phys. Eng. Sci.*, *463*(2088), 3151–3170,
831 doi:10.1098/rspa.2007.1901.

832 Cavaleri, L., B. Fox-Kemper, and M. Hemer (2012), Wind Waves in the Coupled Climate
833 System, *Bull. Am. Meteorol. Soc.*, *93*(11), 1651–1661, doi:10.1175/BAMS-D-11-
834 00170.1.

835 Chameides, W. L., and A. W. Stelson (1992), Aqueous-phase chemical processes in
836 deliquescent sea-salt aerosols: A mechanism that couples the atmospheric cycles
837 of S and sea salt, *J. Geophys. Res. Atmospheres*, *97*(D18), 20565–20580,
838 doi:10.1029/92JD01923.

839 Clarke, A. D., S. R. Owens, and J. Zhou (2006), An ultrafine sea-salt flux from breaking
840 waves: Implications for cloud condensation nuclei in the remote marine
841 atmosphere, *J. Geophys. Res.*, *111*(D6), doi:10.1029/2005JD006565.

842 Clarke, A. D., S. Freitag, R. M. C. Simpson, J. G. Hudson, S. G. Howell, V. L.
843 Brekhovskikh, T. Campos, V. N. Kapustin, and J. Zhou (2013), Free troposphere
844 as a major source of CCN for the equatorial pacific boundary layer: long-range
845 transport and teleconnections, *Atmos Chem Phys*, *13*(15), 7511–7529,
846 doi:10.5194/acp-13-7511-2013.

847 Dentener, F., S. Kinne, T. Bond, O. Boucher, J. Cofala, S. Generoso, P. Ginoux, S. Gong,
848 J. J. Hoelzemann, and A. Ito (2006), Emissions of primary aerosol and precursor
849 gases in the years 2000 and 1750, *Atmos Chem Phys Discuss*, *6*.

Edson, J. B., V. Jampana, R. A. Weller, S. P. Bigorre, A. J. Plueddemann, C. W. Fairall, S. D. Miller, L. Mahrt, D. Vickers, and H. Hersbach (2013), On the Exchange of Momentum over the Open Ocean, *J. Phys. Oceanogr.*, *43*(8), 1589–1610, doi:10.1175/JPO-D-12-0173.1.

Erickson, D. J., C. Seuzaret, W. C. Keene, and S. L. Gong (1999), A general circulation model based calculation of HCl and ClNO2 production from sea salt dechlorination: Reactive Chlorine Emissions Inventory, *J. Geophys. Res. Atmospheres*, *104*(D7), 8347–8372, doi:10.1029/98JD01384.

Facchini, M. C. et al. (2008), Primary submicron marine aerosol dominated by insoluble organic colloids and aggregates, *Geophys. Res. Lett.*, *35*(17), doi:10.1029/2008GL034210.

Fan, Y., I. Ginis, and T. Hara (2010), Momentum Flux Budget across the Air–Sea Interface under Uniform and Tropical Cyclone Winds, *J. Phys. Oceanogr.*, *40*(10), 2221–2242, doi:10.1175/2010JPO4299.1.

Felizardo, F. C., and W. K. Melville (1995), Correlations between Ambient Noise and the Ocean Surface Wave Field, *J. Phys. Oceanogr.*, *25*(4), 513–532, doi:10.1175/1520-0485(1995)025<0513:CBANAT>2.0.CO;2.

Gantt, B., N. Meskhidze, and D. Kamykowski (2009), A new physically-based quantification of marine isoprene and primary organic aerosol emissions, *Atmospheric Chem. Phys.*, *9*(14), 4915–4927, doi:10.5194/acp-9-4915-2009.

Geever, M., C. D. O'Dowd, S. van Ekeren, R. Flanagan, E. D. Nilsson, G. de Leeuw, and Ü. Rannik (2005), Submicron sea spray fluxes, *Geophys. Res. Lett.*, *32*(15), L15810, doi:10.1029/2005GL023081.

Ghan, S. J., and R. A. Zaveri (2007), Parameterization of optical properties for hydrated internally mixed aerosol, *J. Geophys. Res.*, *112*(D10), doi:10.1029/2006JD007927.

Glasow, R. von, and P. J. Crutzen (2004), Model study of multiphase DMS oxidation with a focus on halogens, *Atmospheric Chem. Phys.*, *4*(3), 589–608.

Gong, S. L. (2003), Canadian Aerosol Module: A size-segregated simulation of atmospheric aerosol processes for climate and air quality models 1. Module development, *J. Geophys. Res.*, *108*(D1), doi:10.1029/2001JD002002.

Grythe, H., J. Ström, R. Krejci, P. Quinn, and A. Stohl (2014), A review of sea-spray aerosol source functions using a large global set of sea salt aerosol concentration measurements, *Atmospheric Chem. Phys.*, *14*(3), 1277–1297, doi:10.5194/acp-14-1277-2014.

885 Hanley, K. E., S. E. Belcher, and P. P. Sullivan (2010), A Global Climatology of Wind–
886 Wave Interaction, *J. Phys. Oceanogr.*, *40*(6), 1263–1282,
887 doi:10.1175/2010JPO4377.1.

888 Hanson, J. L., and O. M. Phillips (1999), Wind sea growth and dissipation in the open
889 ocean, *J. Phys. Oceanogr.*, *29*(8), 1633–1648.

890 Hara, T., and S. E. Belcher (2004), Wind Profile and Drag Coefficient over Mature
891 Ocean Surface Wave Spectra, *J. Phys. Oceanogr.*, *34*(11), 2345–2358,
892 doi:10.1175/JPO2633.1.

893 Hoffman, E. J., and R. A. Duce (1976), Factors influencing the organic carbon content of
894 marine aerosols: A laboratory study, *J. Geophys. Res.*, *81*(21), 3667–3670,
895 doi:10.1029/JC081i021p03667.

896 Hoque, A. (2002), Air Bubble Entrainment by Breaking Waves and Associated Energy
897 Dissipation, Toyohashi University of Technology, Japan.

898 Hultin, K. A. H., E. D. Nilsson, R. Krejci, E. M. Mårtensson, M. Ehn, Å. Hagström, and
899 G. de Leeuw (2010), In situ laboratory sea spray production during the Marine
900 Aerosol Production 2006 cruise on the northeastern Atlantic Ocean, *J. Geophys.*
901 *Res. Atmospheres*, *115*(D6), n/a–n/a, doi:10.1029/2009JD012522.

902 Hurrell, J. W. et al. (2013), The Community Earth System Model: A Framework for
903 Collaborative Research, *Bull. Am. Meteorol. Soc.*, *94*(9), 1339–1360,
904 doi:10.1175/BAMS-D-12-00121.1.

905 Hyer, E. J., J. S. Reid, and J. Zhang (2011), An over-land aerosol optical depth data set
906 for data assimilation by filtering, correction, and aggregation of MODIS
907 Collection 5 optical depth retrievals, *Atmos Meas Tech*, *4*(3), 379–408,
908 doi:10.5194/amt-4-379-2011.

909 Jaeglé, L., P. K. Quinn, T. S. Bates, B. Alexander, and J.-T. Lin (2011), Global
910 distribution of sea salt aerosols: new constraints from in situ and remote sensing
911 observations, *Atmospheric Chem. Phys.*, *11*(7), 3137–3157, doi:10.5194/acp-11-
912 3137-2011.

913 Kalnay, E. et al. (1996), The NCEP/NCAR 40-Year Reanalysis Project, *Bull. Am.*
914 *Meteorol. Soc.*, *77*(3), 437–471, doi:10.1175/1520-
915 0477(1996)077<0437:TNYRP>2.0.CO;2.

916 Kaufman, Y. J., D. Tanré, and O. Boucher (2002), A satellite view of aerosols in the
917 climate system, *Nature*, *419*(6903), 215–223.

918 Keene, W. C. et al. (2007), Chemical and physical characteristics of nascent aerosols
919 produced by bursting bubbles at a model air-sea interface, *J. Geophys. Res.*,
920 *112*(D21), doi:10.1029/2007JD008464.

921 Keene, W. C., M. S. Long, A. A. P. Pszenny, R. Sander, J. R. Maben, A. J. Wall, T. L.
922 O'Halloran, A. Kerkweg, E. V. Fischer, and O. Schrems (2009), Latitudinal
923 variation in the multiphase chemical processing of inorganic halogens and related
924 species over the eastern North and South Atlantic Oceans, *Atmospheric Chem.*
925 *Phys.*, *9*(19), 7361–7385.

926 Lamarre, E., and W. K. Melville (1991), Air entrainment and dissipation in breaking
927 waves, *Nature*, *351*(6326), 469–472, doi:10.1038/351469a0.

928 Langmann, B., C. Scannell, and C. O'Dowd (2008), New Directions: Organic matter
929 contribution to marine aerosols and cloud condensation nuclei, *Atmos. Environ.*,
930 *42*, 7821–7822, doi:10.1016/j.atmosenv.2008.09.002.

931 Levy, R. C., S. Mattoo, L. A. Munchak, L. A. Remer, A. M. Sayer, F. Patadia, and N. C.
932 Hsu (2013), The Collection 6 MODIS aerosol products over land and ocean,
933 *Atmos Meas Tech*, *6*(11), 2989–3034, doi:10.5194/amt-6-2989-2013.

934 Liu, X. et al. (2012), Toward a minimal representation of aerosols in climate models:
935 description and evaluation in the Community Atmosphere Model CAM5, *Geosci.*
936 *Model Dev.*, *5*(3), 709–739, doi:10.5194/gmd-5-709-2012.

937 Loewen, M. R., and W. K. Melville (1994), An experimental investigation of the
938 collective oscillations of bubble plumes entrained by breaking waves, *J. Acoust.*
939 *Soc. Am.*, *95*(3), 1329–1343, doi:10.1121/1.408573.

940 Long, M. S., W. C. Keene, D. J. Kieber, D. J. Erickson, and H. Maring (2011), A sea-
941 state based source function for size- and composition-resolved marine aerosol
942 production, *Atmospheric Chem. Phys.*, *11*(3), 1203–1216, doi:10.5194/acp-11-
943 1203-2011.

944 Long, M. S., W. C. Keene, R. C. Easter, R. Sander, X. Liu, A. Kerkweg, and D. Erickson
945 (2013), Sensitivity of tropospheric chemical composition to halogen-radical
946 chemistry using a fully coupled size-resolved multiphase chemistry/global climate
947 system – Part 1: Halogen distributions, aerosol composition, and sensitivity of
948 climate-relevant gases, *Atmospheric Chem. Phys. Discuss.*, *13*(3), 6067–6129,
949 doi:10.5194/acpd-13-6067-2013.

950 Long, M. S., W. C. Keene, D. J. Kieber, A. A. Frossard, L. M. Russell, J. R. Maben, J. D.
951 Kinsey, P. K. Quinn, and T. S. Bates (2014), Light-enhanced primary marine
952 aerosol production from biologically productive seawater, *Geophys. Res. Lett.*,
953 2014GL059436, doi:10.1002/2014GL059436.

954 Mårtensson, E. M., E. D. Nilsson, G. de Leeuw, L. H. Cohen, and H.-C. Hansson (2003),
955 Laboratory simulations and parameterization of the primary marine aerosol
956 production, *J. Geophys. Res. Atmospheres*, *108*(D9), 4297,
957 doi:10.1029/2002JD002263.

Modini, R. L., L. M. Russell, G. B. Deane, and M. D. Stokes (2013), Effect of soluble surfactant on bubble persistence and bubble-produced aerosol particles, *J. Geophys. Res. Atmospheres*, *118*(3), 1388–1400, doi:10.1002/jgrd.50186.

Monahan, E. C., and I. G. O'Muircheartaigh (1986), Whitecaps and the passive remote sensing of the ocean surface, *Int. J. Remote Sens.*, *7*(5), 627–642, doi:10.1080/01431168608954716.

Monahan, E. C., D. E. Spiel, and K. L. Davidson (1986), A Model of Marine Aerosol Generation Via Whitecaps and Wave Disruption, in *Oceanic Whitecaps*, vol. 2, edited by E. Monahan and G. Niocaill, pp. 167–174, Springer Netherlands.

Norris, S. J., I. M. Brooks, and D. J. Salisbury (2013), A wave roughness Reynolds number parameterization of the sea spray source flux, *Geophys. Res. Lett.*, *40*(16), 4415–4419, doi:10.1002/grl.50795.

Partanen, A.-I. et al. (2014), Global modelling of direct and indirect effects of sea spray aerosol using a source function encapsulating wave state, *Atmos Chem Phys*, *14*(21), 11731–11752, doi:10.5194/acp-14-11731-2014.

Pierce, J. R., and P. J. Adams (2006), Global evaluation of CCN formation by direct emission of sea salt and growth of ultrafine sea salt, *J. Geophys. Res.*, *111*(D6), doi:10.1029/2005JD006186.

Quinn, P. K., T. S. Bates, K. S. Schulz, D. J. Coffman, A. A. Frossard, L. M. Russell, W. C. Keene, and D. J. Kieber (2014), Contribution of sea surface carbon pool to organic matter enrichment in sea spray aerosol, *Nat. Geosci.*, *7*(3), 228–232, doi:10.1038/ngeo2092.

Reid, J. S., H. H. Jonsson, M. H. Smith, and A. Smirnov (2001), Evolution of the vertical profile and flux of large sea-salt particles in a coastal zone, *J. Geophys. Res. Atmospheres*, *106*(D11), 12039–12053, doi:10.1029/2000JD900848.

Reid, J. S., B. Brooks, K. K. Crahan, D. A. Hegg, T. F. Eck, N. O'Neill, G. de Leeuw, E. A. Reid, and K. D. Anderson (2006), Reconciliation of coarse mode sea-salt aerosol particle size measurements and parameterizations at a subtropical ocean receptor site, *J. Geophys. Res.*, *111*(D2), doi:10.1029/2005JD006200.

Reynolds, R. W., N. A. Rayner, T. M. Smith, D. C. Stokes, and W. Wang (2002), An Improved In Situ and Satellite SST Analysis for Climate, *J. Clim.*, *15*(13), 1609–1625, doi:10.1175/1520-0442(2002)015<1609:AIISAS>2.0.CO;2.

Reynolds, R. W., T. M. Smith, C. Liu, D. B. Chelton, K. S. Casey, and M. G. Schlax (2007), Daily High-Resolution-Blended Analyses for Sea Surface Temperature, *J. Clim.*, *20*(22), 5473–5496, doi:10.1175/2007JCLI1824.1.

993 Rinaldi, M. et al. (2013), Is chlorophyll-a the best surrogate for organic matter
994 enrichment in submicron primary marine aerosol?, *J. Geophys. Res. Atmospheres*,
995 *118*(10), 4964–4973, doi:10.1002/jgrd.50417.

996 Roelofs, G. J. (2008), A GCM study of organic matter in marine aerosol and its potential
997 contribution to cloud drop activation, *Atmospheric Chem. Phys.*, *8*(3), 709–719.

998 Savoie, D. L., and J. M. Prospero (1977), Aerosol concentration statistics for the
999 Northern Tropical Atlantic, *J. Geophys. Res.*, *82*(37), 5954–5964,
1000 doi:10.1029/JC082i037p05954.

1001 Sellegri, K., C. D. O'Dowd, Y. J. Yoon, S. G. Jennings, and G. de Leeuw (2006),
1002 Surfactants and submicron sea spray generation, *J. Geophys. Res.*, *111*(D22),
1003 doi:10.1029/2005JD006658.

1004 Shi, Y., J. Zhang, J. S. Reid, B. Holben, E. J. Hyer, and C. Curtis (2011), An analysis of
1005 the collection 5 MODIS over-ocean aerosol optical depth product for its
1006 implication in aerosol assimilation, *Atmos Chem Phys*, *11*(2), 557–565,
1007 doi:10.5194/acp-11-557-2011.

1008 Shi, Y., J. Zhang, J. S. Reid, E. J. Hyer, T. M. McHardy, and L. Lee (2014), Evaluating
1009 MODIS Collection 6 Dark Target Over Water Aerosol Products for Multi-sensor
1010 Data Fusion, *AGU Fall Meet. Abstr.*, *-1*, 3093.

1011 Spracklen, D. V. et al. (2008), Contribution of particle formation to global cloud
1012 condensation nuclei concentrations, *Geophys. Res. Lett.*, *35*(6),
1013 doi:10.1029/2007GL033038.

1014 Textor, C., M. Schulz, S. Guibert, S. Kinne, Y. Balkanski, S. Bauer, T. Berntsen, T.
1015 Berglen, O. Boucher, and M. Chin (2006), Analysis and quantification of the
1016 diversities of aerosol life cycles within AeroCom, *Atmospheric Chem. Phys.*, *6*(7),
1017 1777–1813.

1018 Tolman, H. L. (2009), *User manual and system documentation of WAVEWATCH III*
1019 *version 3.14*.

1020 Tolman, H. L., and D. Chalikov (1996), Source Terms in a Third-Generation Wind Wave
1021 Model, *J. Phys. Oceanogr.*, *26*(11), 2497–2518, doi:10.1175/1520-
1022 0485(1996)026<2497:STIATG>2.0.CO;2.

1023 Tyree, C. A., V. M. Hellion, O. A. Alexandrova, and J. O. Allen (2007), Foam droplets
1024 generated from natural and artificial seawaters, *J. Geophys. Res.*, *112*(D12),
1025 doi:10.1029/2006JD007729.

1026 Vey, S., R. Dietrich, A. Rülke, M. Fritsche, P. Steigenberger, and M. Rothacher (2009),
1027 Validation of Precipitable Water Vapor within the NCEP/DOE Reanalysis Using
1028 Global GPS Observations from One Decade, *J. Clim.*, *23*(7), 1675–1695,
1029 doi:10.1175/2009JCLI2787.1.

1030 Webb, A., and B. Fox-Kemper (2011), Wave spectral moments and Stokes drift
1031 estimation, *Ocean Model.*, *40*(3–4), 273–288, doi:10.1016/j.ocemod.2011.08.007.

1032 Zhang, J., and J. S. Reid (2009), An analysis of clear sky and contextual biases using an
1033 operational over ocean MODIS aerosol product, *Geophys. Res. Lett.*, *36*(15),
1034 L15824, doi:10.1029/2009GL038723.

1035 Zhang, J., J. S. Reid, D. L. Westphal, N. L. Baker, and E. J. Hyer (2008), A system for
1036 operational aerosol optical depth data assimilation over global oceans, *J.*
1037 *Geophys. Res. Atmospheres*, *113*(D10), D10208, doi:10.1029/2007JD009065.

1038 Zhang, J., J. R. Campbell, E. J. Hyer, J. S. Reid, D. L. Westphal, and R. S. Johnson
1039 (2014), Evaluating the impact of multisensor data assimilation on a global aerosol
1040 particle transport model, *J. Geophys. Res. Atmospheres*, *119*(8), 2013JD020975,
1041 doi:10.1002/2013JD020975.

1042 Zhou, X., A. J. Davis, D. J. Kieber, W. C. Keene, J. R. Maben, H. Maring, E. E. Dahl, M.
1043 A. Izaguirre, R. Sander, and L. Smoydzyn (2008), Photochemical production of
1044 hydroxyl radical and hydroperoxides in water extracts of nascent marine aerosols
1045 produced by bursting bubbles from Sargasso seawater, *Geophys. Res. Lett.*,
1046 *35*(20), doi:10.1029/2008GL035418.

1047

Figure Legends

Figure 1. Size-resolved number production fluxes based on (a) STD-U_{10} at U_{10} = 9 m s^{-1} and WAVE at an equivalent F_{Det} = 6.3 x 10^{-5} m s^{-1} and (b) STD-WAVE, STD-WAVE scaled by 0.075 per Section 3.1, and WAVE at ε_d = 0.16 J m^{-2} s^{-1} (equivalent to U_{10} = 9 m s^{-1} and F_{Det} = 6.4 x 10^{-5} m s^{-1}).

Figure 2. Simulated energy dissipation flux due to wave breaking (ε_d) versus U_{10} for (a) the Pacific Ocean from 30S – 29N (green) and from 30 -70N (blue), (b) the Indian Ocean from 30S to 30N, (c) the Atlantic Ocean from 30S – 29N (dark green) and from 30 -70N (light green), and (d) the Southern Ocean below 30S latitude. The black lines depict regressions from Hanson and Phillips [1999], $\varepsilon_d = 4.28 \times 10^{-5} U_{10}^{3.74}$.

Figure 3. PMA number and mass production fluxes simulated with STD-U_{10} (a and b, respectively) and WAVE (c and d, respectively) and the corresponding fractional differences expressed as percent ((WAVE – STD-U10) / WAVE) (e and f, respectively).

Figure 4. PMA number and mass production fluxes simulated with STD-WAVE (a and b, respectively) and the corresponding fractional differences relative to STD-U_{10} expressed as percent ((STD-WAVE – STD-U_{10}) / STD-WAVE) (c and d, respectively).

Figure 5. NaCl mass concentration in the surface layer simulated with (a) STD-U_{10} and (b) STD-WAVE and (c) the corresponding percent relative difference.

Figure 6. PMA number and mass production fluxes simulated with STD-$WAVE_{291K}$ (a and b, respectively) and the corresponding fractional differences relative to STD-WAVE expressed as percent ((STD-$WAVE_{291K}$ – STD-WAVE) / STD-$WAVE_{291K}$) (c and d, respectively).

Figure 7. Comparison of annual average Na^+ concentrations simulated with STD-U_{10}, STD-WAVE, and STD-$WAVE_{291K}$ for the lowest model level versus those from the AEROCE, SEAREX and DOE-EML (Section 2.5.2) measurement programs (a, c, and e, respectively), and the corresponding ratio of average modeled to measured Na^+ concentrations versus modeled U_{10} (b, d, and f, respectively).

Figure 8. Average AOD simulated with (a) STD-U_{10} and (b) STD-WAVE, (c) AOD retrieved from MODIS-Aqua/Terra, and (d) the corresponding ratio of AOD

simulated with STD-WAVE (from panel (b) versus measured AOD (from panel (c). White regions in (a-c) indicate regions where no MODIS data were available. White regions in (d) correspond to those for which all MODIS data were excluded based on criteria described in Section 2.5.3.

Figure 9. Annually averaged percent bias in model (STD-$WAVE_{291K}$) RH compared to NCEP reanalysis for 2002-2006 at (a) the surface and (b) 850 hPa.

Figure 10. Ratio of observed to modeled average annual concentrations of Na^+ in near surface air. Measurements are from the AEROCE, SEAREX and DOE-EML (Section 2.5.2) programs to simulated with STD-U_{10}, STD-WAVE, and STE-$WAVE_{291K}$ versus model SST. The red line is the regression from Jaeglé et al. [2011].

Figure 11. Na^+ mass flux vs. SST (^oC) for (a) STD-U_{10}, (b) STD-WAVE, (c) STD-$WAVE_{291K}$, and the corresponding ratio wave model to STD-U_{10} Na^+ for (d) STD-WAVE and (e) STD-$WAVE_{291K}$.

Figure 12. Ratio of observed to modeled AOD for (f) STD-U_{10}, (g) STD-WAVE, and (h) STD-$WAVE_{291K}$ and the corresponding ratio wave model to STD-U_{10} AOD for (d) STD-WAVE and (e) STD-$WAVE_{291K}$. The green line in (h) depicts the polynomial regression reported by Jaeglé et al. [2011].

Figure 13. Ratios of observed to modeled AOD (top) and surface Na^+ concentration (bottom) for STD-$WAVE_{291K}$ versus chlorophyll *a*.

Figure 1. Size-resolved number production fluxes based on (a) STD-U_{10} at U_{10} = 9 m s^{-1} and WAVE at an equivalent F_{Det} = 6.3 x 10^{-5} m s^{-1} and (b) STD-WAVE, STD-WAVE scaled by 0.075 per Section 3.1, and WAVE at ε_d = 0.16 J m^{-2} s^{-1} (equivalent to U_{10} = 9 m s^{-1} and F_{Det} = 6.4 x 10^{-5} m s^{-1}).

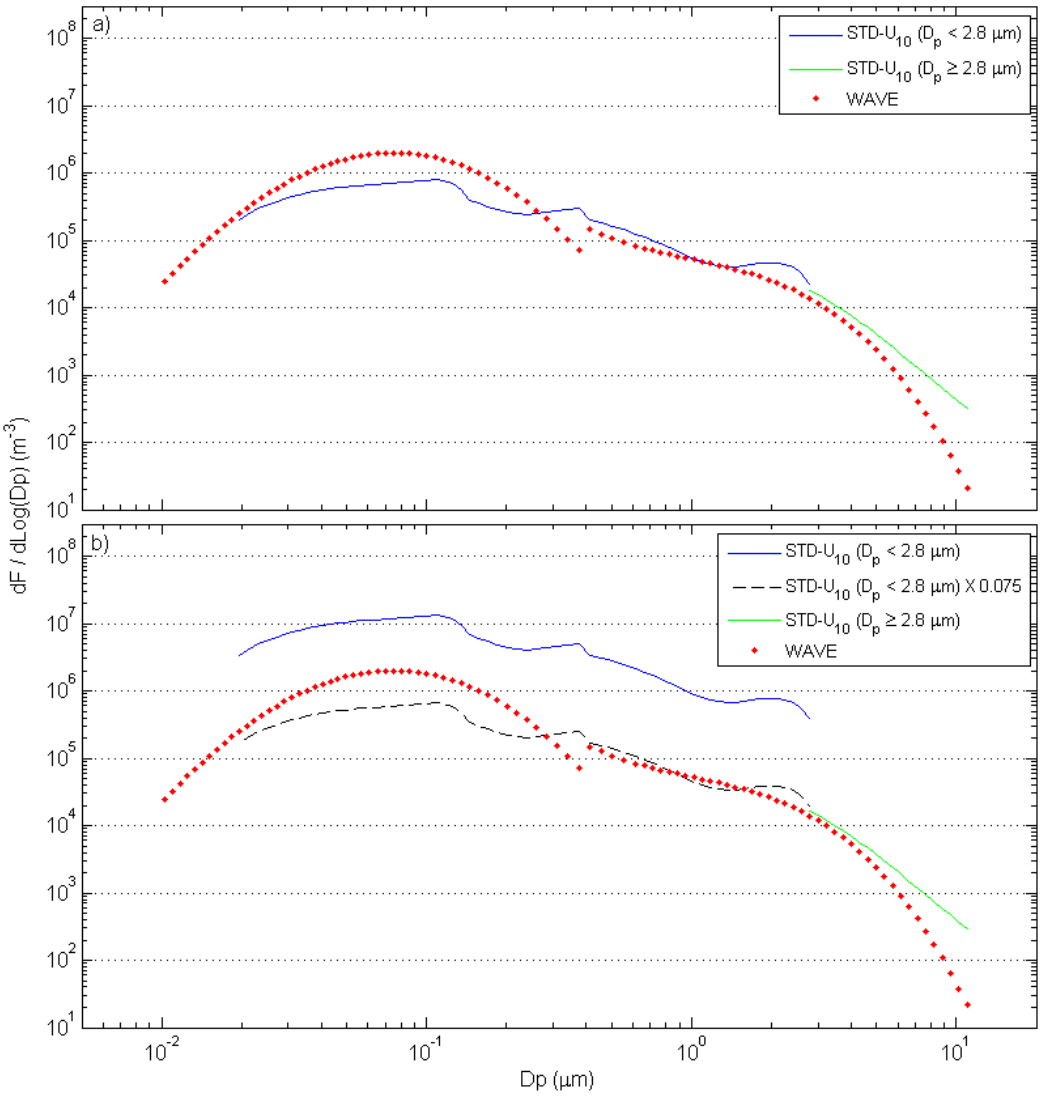

Figure 2. Simulated energy dissipation flux due to wave breaking (ε_d) versus U_{10} for (a) the Pacific Ocean from 30S – 29N (green) and from 30 -70N (blue), (b) the Indian Ocean from 30S to 30N, (c) the Atlantic Ocean from 30S – 29N (dark green) and from 30 -70N (light green), and (d) the Southern Ocean below 30S latitude. The black lines depict regressions from Hanson and Phillips [1999], $\varepsilon_d = 4.28 \times 10^{-5} U_{10}^{3.74}$.

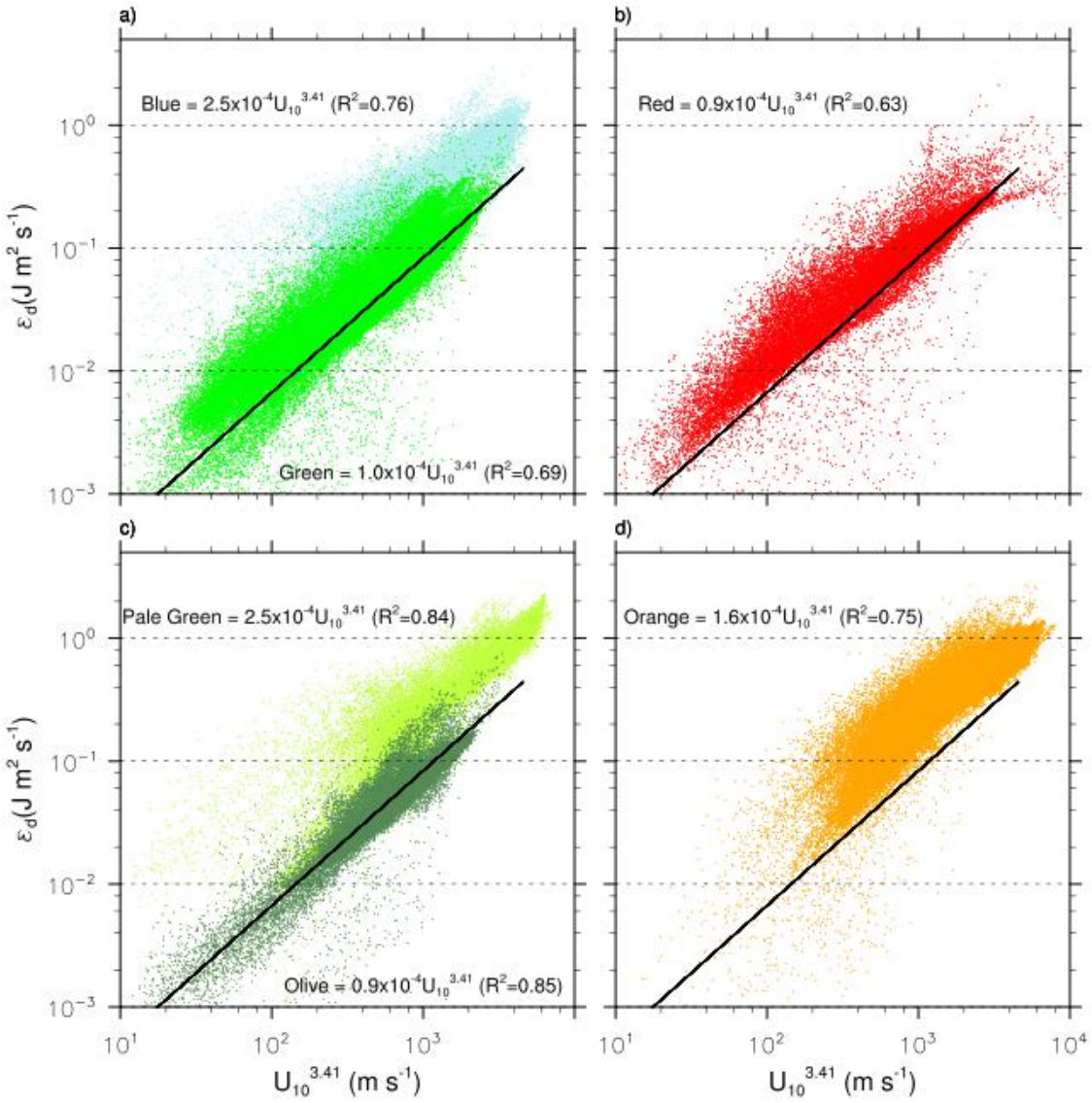

Figure 3. PMA number and mass production fluxes simulated with STD-U_{10} (a and b, respectively) and WAVE (c and d, respectively) and the corresponding fractional differences expressed as percent ((WAVE – STD-U10) / WAVE) (e and f, respectively).

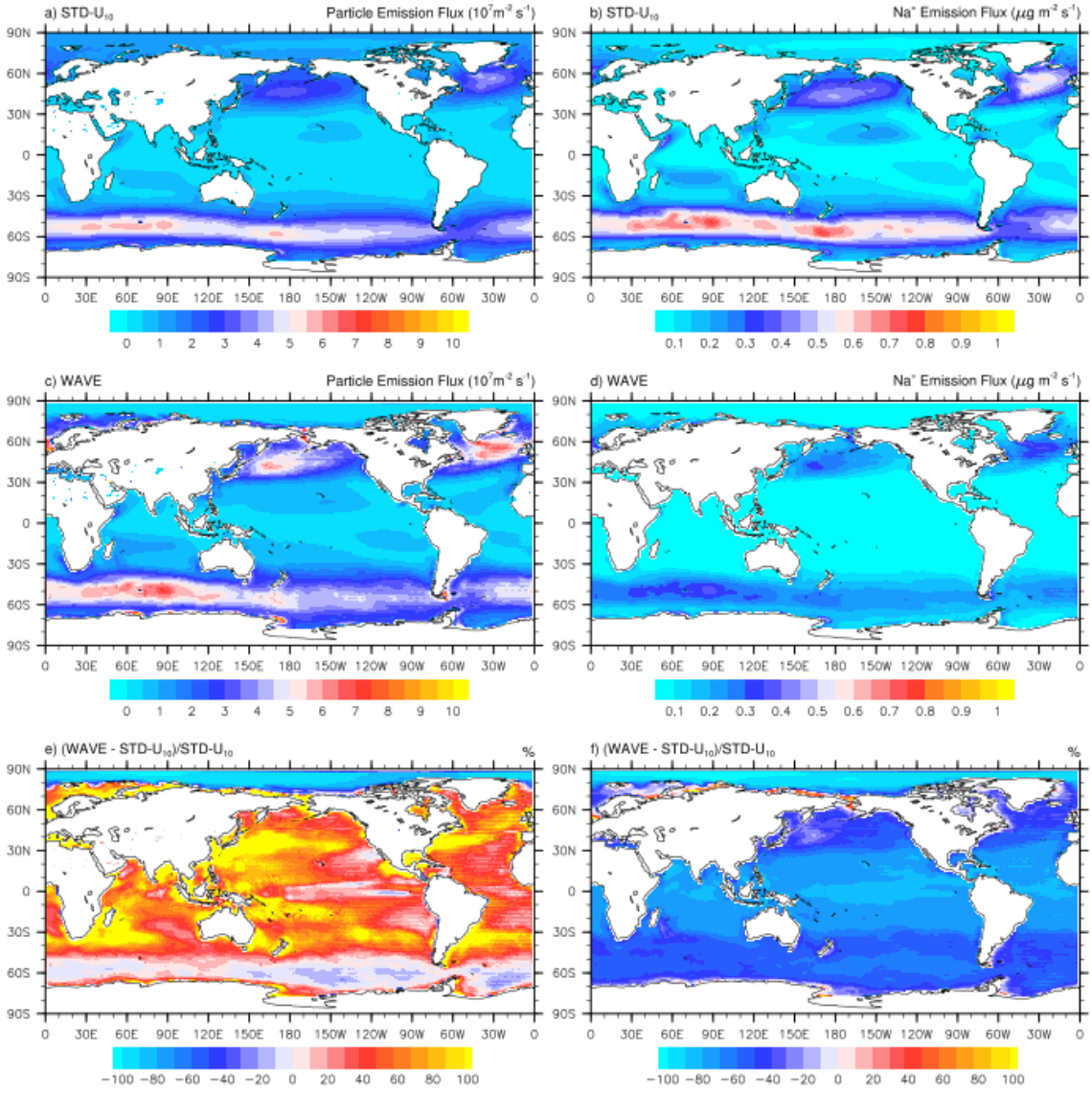

Figure 4. PMA number and mass production fluxes simulated with STD-WAVE (a and b, respectively) and the corresponding fractional differences relative to STD-U_{10} expressed as percent ((STD-WAVE – STD-U_{10}) / STD-WAVE) (c and d, respectively).

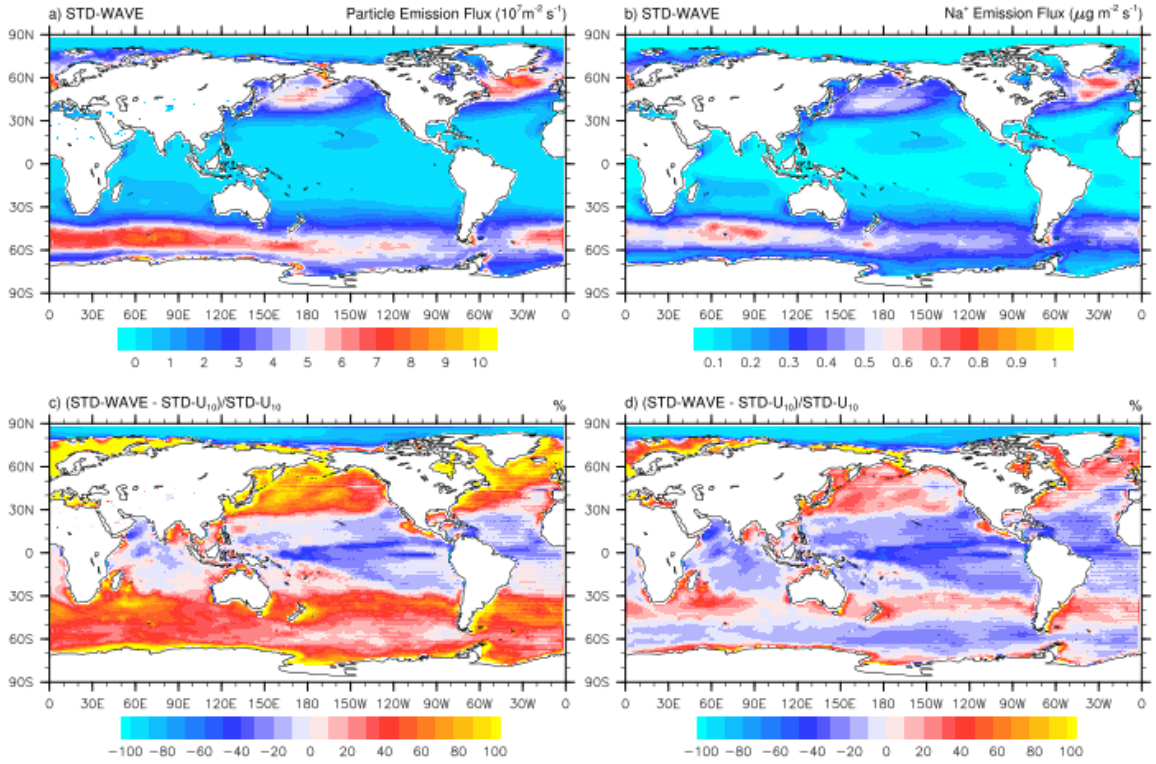

Figure 5. NaCl mass concentration in the surface layer simulated with (a) STD-U_{10} and (b) STD-WAVE and (c) the corresponding percent relative difference.

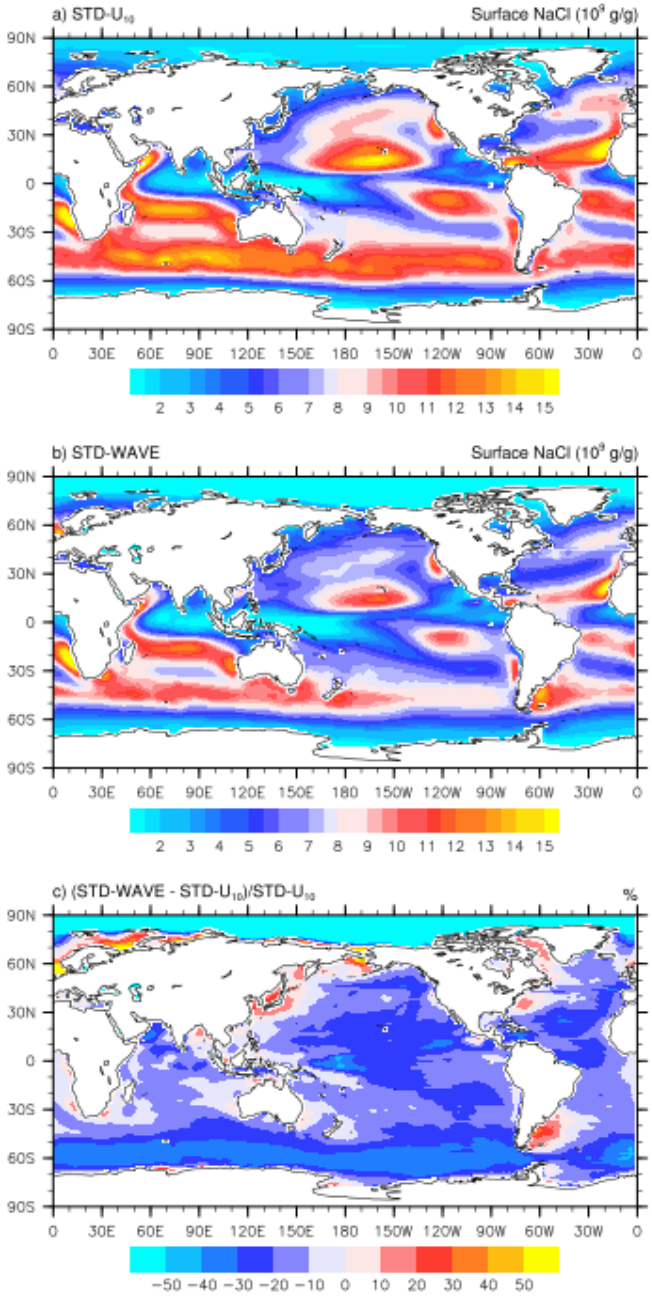

Figure 6. PMA number and mass production fluxes simulated with STD-WAVE$_{291K}$ (a and b, respectively) and the corresponding fractional differences relative to STD-WAVE expressed as percent ((STD-WAVE$_{291K}$ – STD-WAVE) / STD-WAVE$_{291K}$) (c and d, respectively).

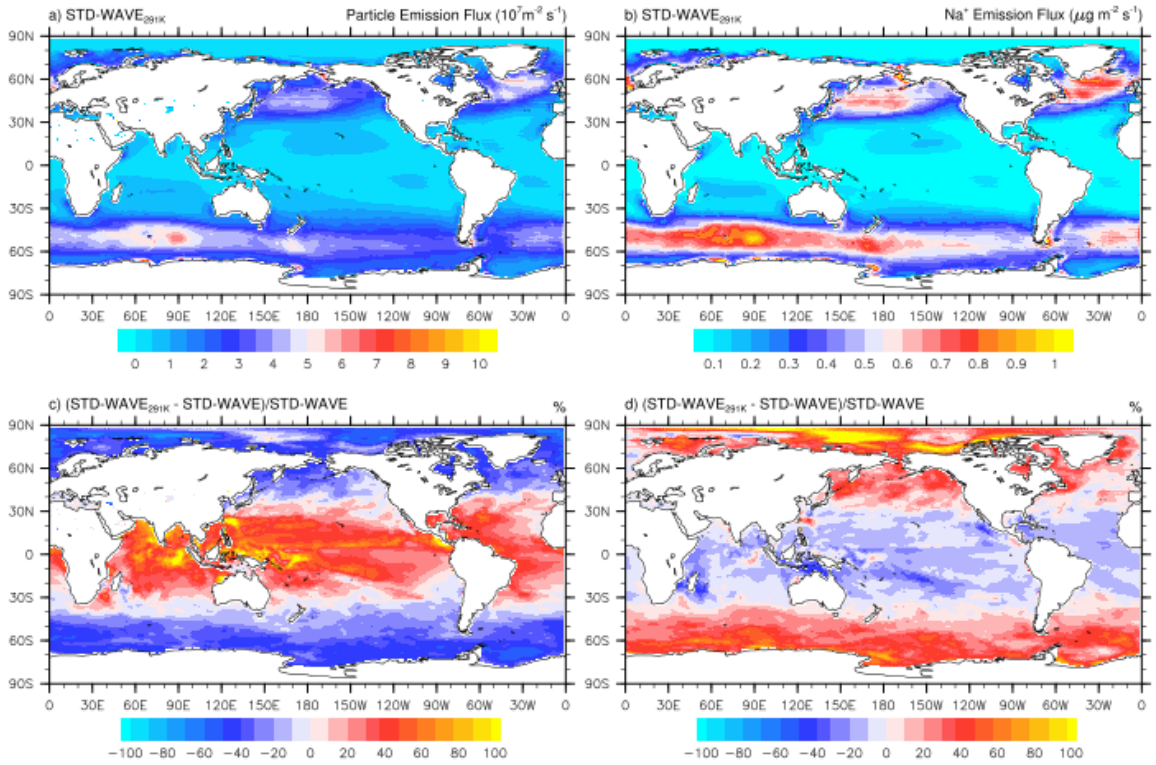

Figure 7. Comparison of annual average Na^+ concentrations simulated with STD-U_{10}, STD-WAVE, and STD-$WAVE_{291K}$ for the lowest model level versus those from the AEROCE, SEAREX and DOE-EML (Section 2.5.2) measurement programs (a, c, and e, respectively), and the corresponding ratio of average modeled to measured Na^+ concentrations versus modeled U_{10} (b, d, and f, respectively).

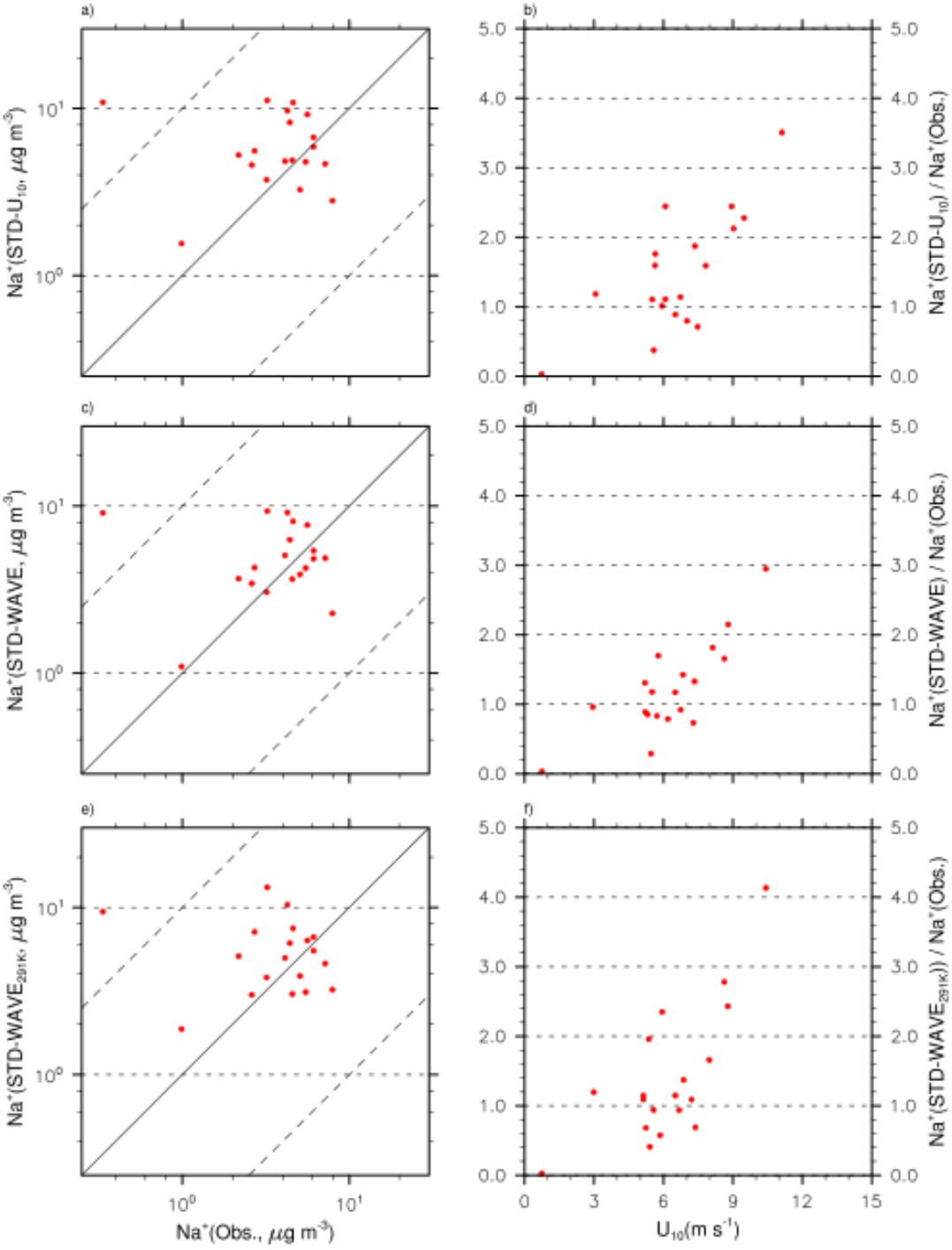

Figure 8. Average AOD simulated with (a) STD-U_{10} and (b) STD-WAVE, (c) AOD retrieved from MODIS-Aqua/Terra, and (d) the corresponding ratio of AOD simulated with STD-WAVE (from panel (b) versus measured AOD (from panel (c). White regions in (a-c) indicate regions where no MODIS data were available. White regions in (d) correspond to those for which all MODIS data were excluded based on criteria described in Section 2.5.3.

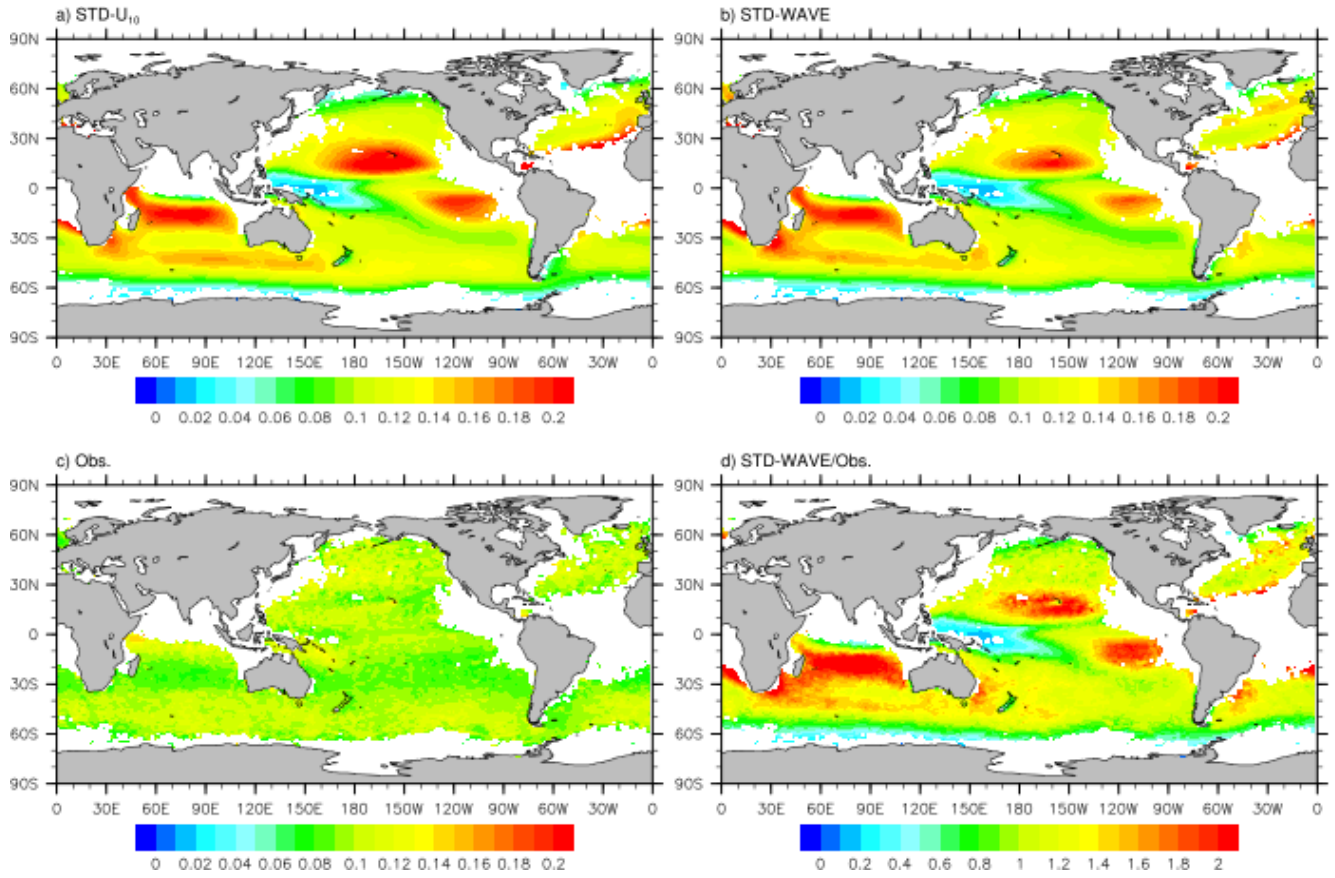

Figure 9. Annually averaged percent bias in model (STD-WAVE$_{291K}$) RH compared to NCEP reanalysis for 2002-2006 at (a) the surface and (b) 850 hPa.

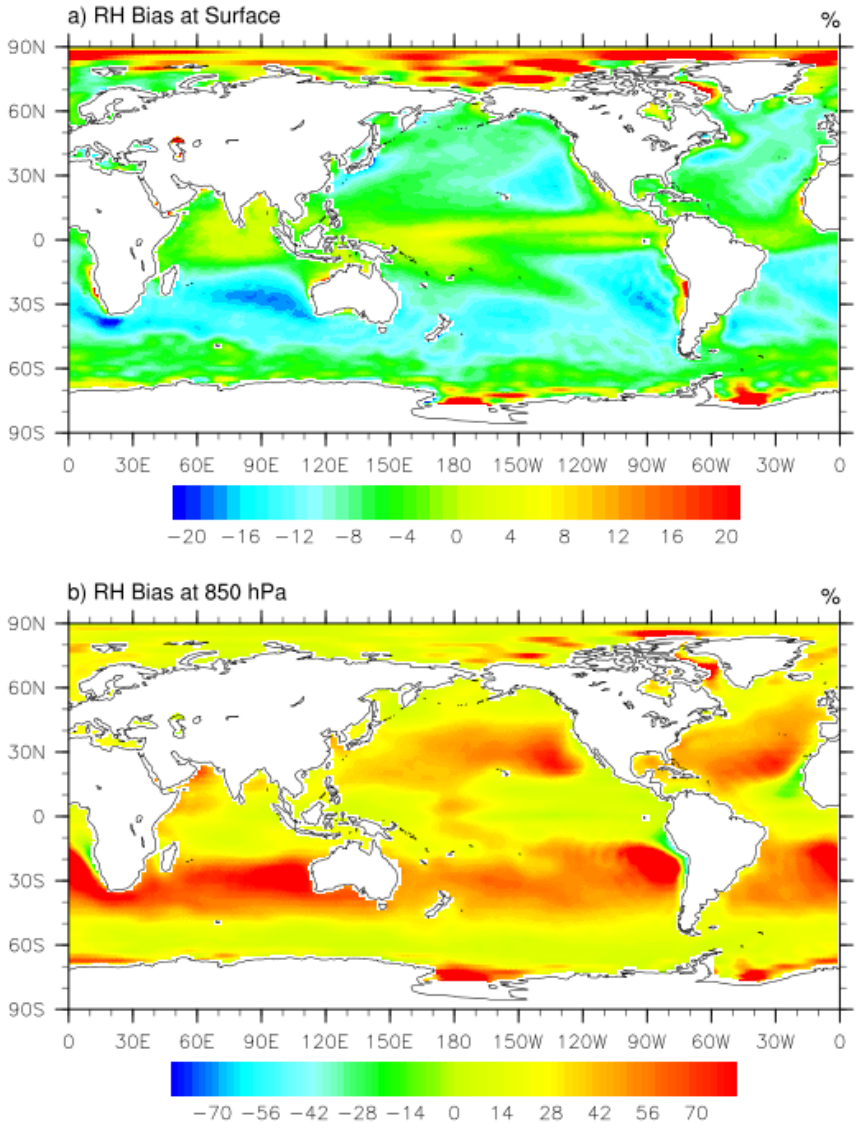

Figure 10. Ratio of observed to modeled average annual concentrations of Na^+ in near surface air. Measurements are from the AEROCE, SEAREX and DOE-EML (Section 2.5.2) programs to simulated with STD-U_{10}, STD-WAVE, and STE-$WAVE_{291K}$ versus model SST. The red line is the regression from *Jaeglé et al.* [2011].

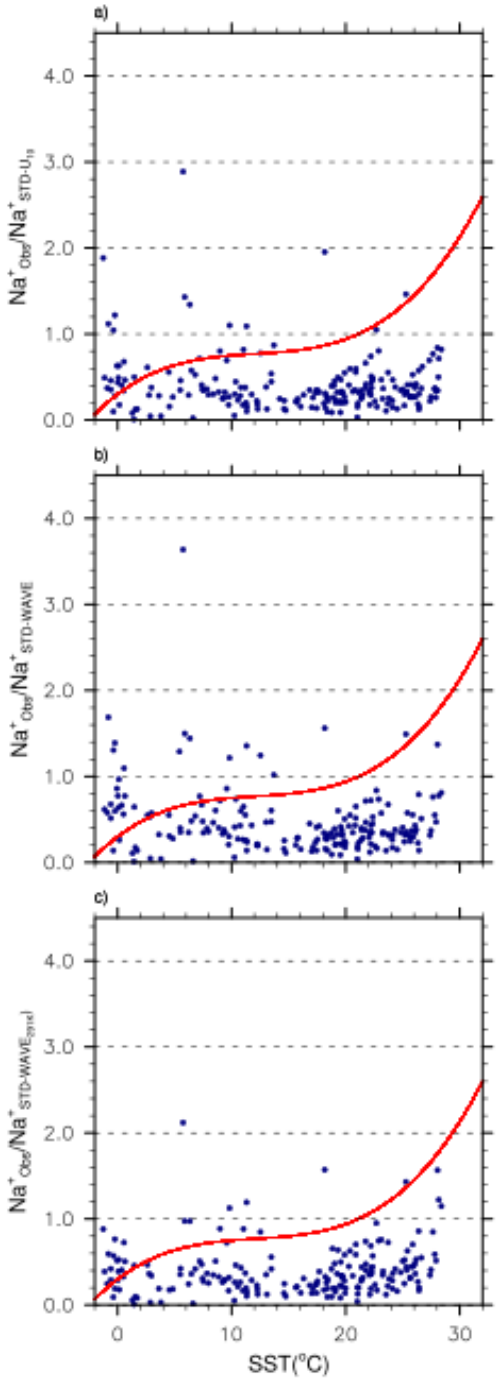

Figure 11. Na^+ mass flux vs. SST (ºC) for (a) STD-U_{10}, (b) STD-WAVE, (c) STD-$WAVE_{291K}$, and the corresponding ratio wave model to STD-U_{10} Na^+ for (d) STD-WAVE and (e) STD-$WAVE_{291K}$.

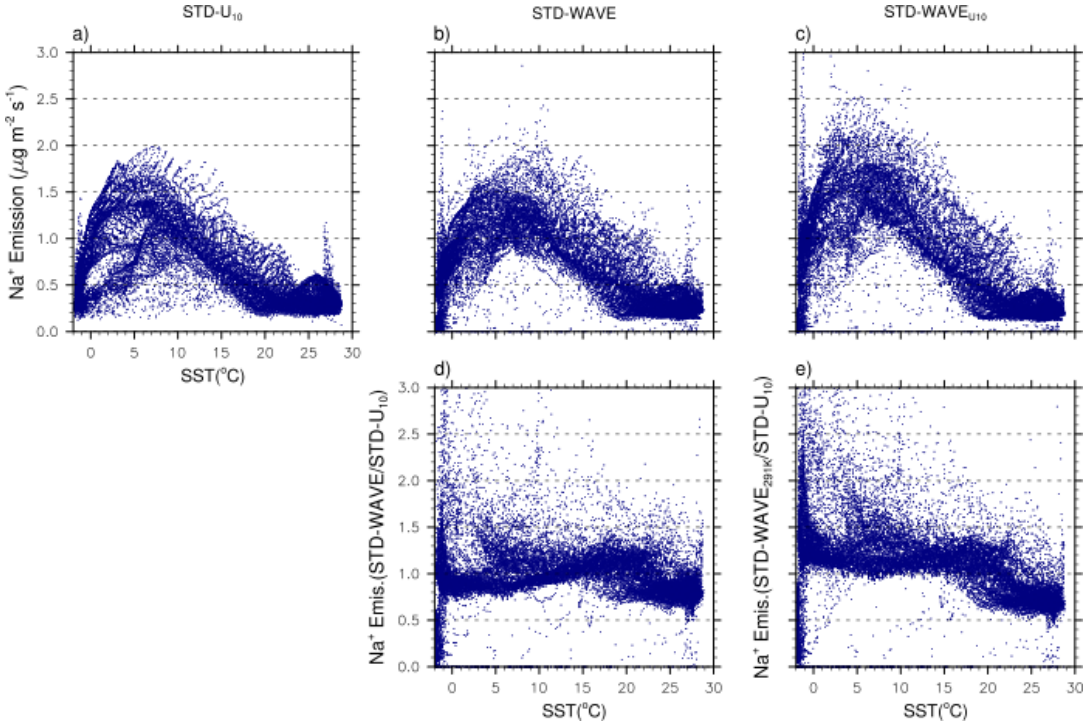

Figure 12. Ratio of observed to modeled AOD for (f) STD-U_{10}, (g) STD-WAVE, and (h) STD-$WAVE_{291K}$ and the corresponding ratio wave model to STD-U_{10} AOD for (d) STD-WAVE and (e) STD-$WAVE_{291K}$. The green line in (h) depicts the polynomial regression reported by Jaeglé et al. [2011].

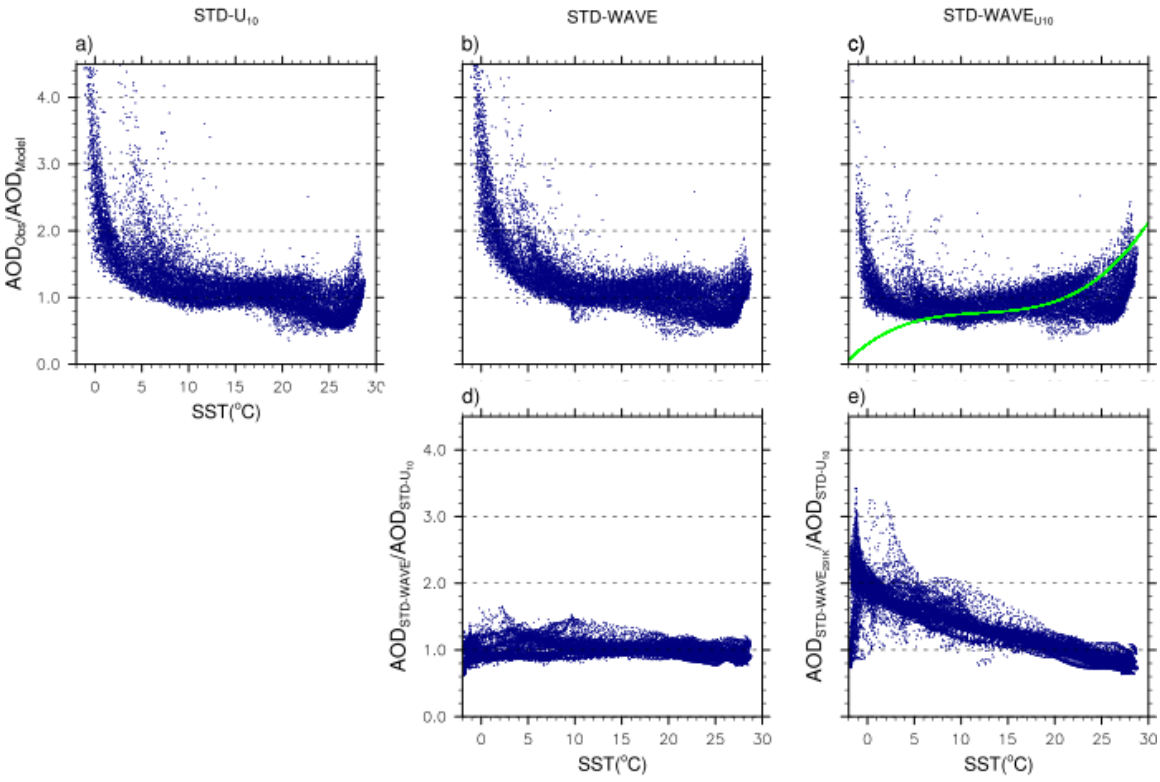

Figure 13. Ratios of observed to modeled AOD (top) and surface Na^+ concentration (bottom) for STD-$WAVE_{291K}$ versus chlorophyll *a*.

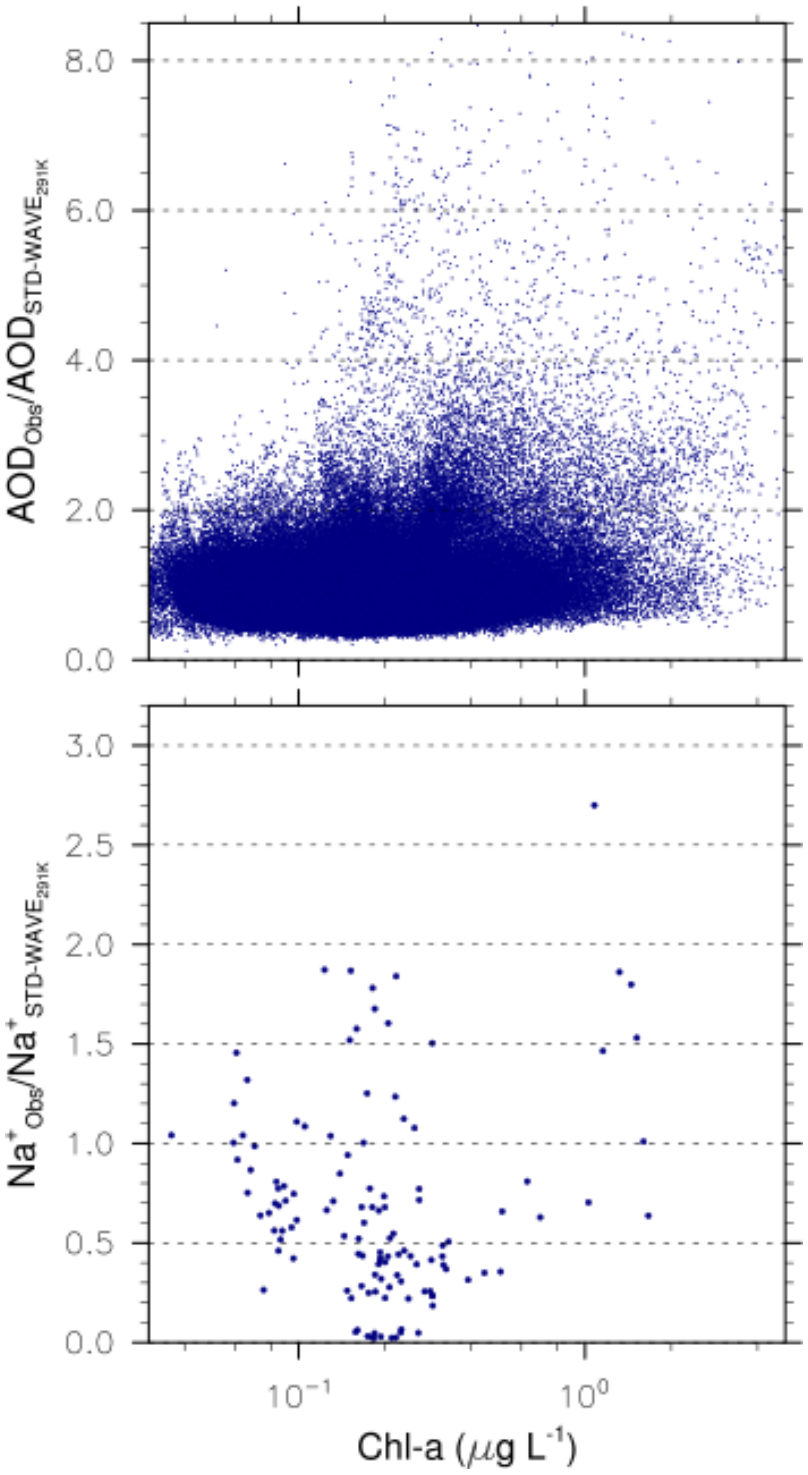

Table 1. Global annual mean particle number production flux; number concentration; and Na^+ production flux, burden, lifetime, and dry- and wet-deposition fluxes compared with published results based on other marine aerosol source functions (adapted from [*Long et al.*, 2014a]. Uncertainties correspond to year-over-year standard deviation for the 5-year annual mean.

Source Function	Number Flux 10^6 m^{-2} s^{-1}	Number Conc. (Range) (cm^{-3})	Na^+ Source (10^3 Tg y^{-1})	Na^+ Burden (Tg)	Na^+ Lifetime (d)	Na^+ Dry Dep. (10^3 Tg y^{-1})	Na^+ Wet Dep. (10^3 Tg y^{-1})
STD-U_{10} (this work)	0.89 ± 0.01	138 ($1.8x10^0$ – $4.7x10^4$)	2.3 ± 0.07	3.7 ± 0.16	0.60 ± 0.01	1.1 ± 0.01	1.2 ± 0.01
WAVE (this work)	1.20 ± 0.02	158 ($2.3x10^0$ – $4.8x10^4$)	1.0 ± 0.01	0.74 ± 0.03	0.26 ± >0.01	0.74 ± 0.01	0.28 ± 0.01
STD-WAVE (this work)	1.24 ± 0.03	148 ($1.4x10^0$ – $4.8x10^4$)	2.3 ± 0.09	3.2 ± 0.11	0.51 ± 0.01	1.2 ± 0.01	1.1 ± 0.01
STD-$WAVE_{291K}$ (this work)	1.00 ± 0.01	141 ($0.6x10^0$ – $4.7x10^4$)	2.6 ± 0.07	3.4 ± 0.12	0.49 ± 0.01	1.3 ± 0.01	1.3 ± 0.01
Long et al., 2011[a]		266 ($4.0x10^0$ – $4.4x10^4$)	1.1 ± 0.02	2.5 ± 0.03	0.86 ± 0.01	0.49 ± 0.01	0.56 ± 0.01
Monahan et al., 1986[b]			1.7	2.4	0.5	0.76	0.90
Various [c]			1.6	2.4	0.5		
Clarke et al., 2006[d]			2.2	4.0	0.66	1.5	0.68
Mårtensson et al., 2003[d]			1.7	0.55	1.2	0.061	0.11
O'Dowd et al., 1997[d]			4.1	5.2	0.47	2.9	1.2
Monahan et al., 1986[d]			0.55	1.2	0.79	0.34	0.19

[a] As reported in Long et al. [2014a].

[b] From reported in Kerkweg et al. [2008].

[c] From Textor et al. [2006].

[d] From Pierce and Adams [2006], Table 2